Title

Axial variation of deoxyhemoglobin density as a source of the low-frequency time lag structure in blood oxygenation level-dependent signals

Authors

Toshihiko Aso[1,2*], Shinnichi Urayama[2,3], Fukuyama Hidenao[2,3], Toshiya Murai[1]

Affiliations

[1]Department of Psychiatry, Kyoto University Graduate School of Medicine, Shogoin-kawaharacho 54, Sakyo-ku, Kyoto, Japan

[2]Human Brain Research Center, Kyoto University Graduate School of Medicine, Shogoin-kawaharacho 54, Sakyo-ku, Kyoto, Japan

[3]Research and Educational Unit of Leaders for Integrated Medical System, Center for the Promotion of Interdisciplinary Education and Research, Kyoto University, Yoshida-honmachi, Sakyo-ku, Kyoto, Japan

*** Correspondence:**

Toshihiko Aso
aso.toshihiko@gmail.com

Running title: Axial variation of deoxy-Hb density as a low-frequency time lag structure source

Keywords

Magnetic resonance imaging, Respiratory control, Cerebral blood flow, Neurovascular coupling, Resting-state fMRI, Vasomotion

Abstract

Perfusion-related information is reportedly embedded in the low-frequency component of a blood oxygen level-dependent (BOLD) functional magnetic resonance imaging (fMRI) signal. The blood-propagation pattern through the cerebral vascular tree is detected as an interregional lag variation of spontaneous low-frequency oscillations (sLFOs). Mapping of this lag, or phase, has been implicitly treated as a projection of the vascular tree structure onto real space. While accumulating evidence supports the biological significance of this signal component, the physiological basis of the "perfusion lag structure," a requirement for an integrative resting-state fMRI-signal model, is lacking. In this study, we conducted analyses furthering the hypothesis that the sLFO is not only largely of systemic origin, but also essentially intrinsic to blood, and hence behaves as a virtual tracer. By summing the small fluctuations of instantaneous phase differences between adjacent vascular regions, a velocity response to respiratory challenges was detected. Regarding the relationship to neurovascular coupling, the removal of the whole lag structure, which can be considered as an optimized global-signal regression, resulted in a reduction of inter-individual variance while preserving the fMRI response. Examination of the T2* and S_0, or non-BOLD, components of the fMRI signal revealed that the lag structure is deoxyhemoglobin dependent, while paradoxically presenting a signal-magnitude reduction in the venous side of the cerebral vasculature. These findings provide insight into the origin of BOLD sLFOs, suggesting that they are highly intrinsic to the circulating blood.

1 Introduction

In functional magnetic resonance imaging (fMRI), there are 2 established physiological bases of signal change: neurovascular coupling (NVC) and autoregulation. The former involves a local blood flow increase of 30–70% which gives rise to a 0.5–2% blood

oxygenation level-dependent (BOLD) signal increase with around a 5-s delay (Buxton, 2013). This is the target phenomenon of fMRI as a tool for brain mapping, due to its limited spatial extent mainly involving local arterioles (Hillman, 2014). In contrast, autoregulatory responses in vessel diameter are found in a wide range of arteries including the internal carotid or middle cerebral arteries (Hoiland *et al.*, 2016). Detection of a compromised response in vascular disorders has proven useful for clinical purposes (Murphy *et al.*, 2011). Importantly, there is no clear physiological distinction between these 2 phenomena as each involves multiple pathways (Willie *et al.*, 2014). Their traces in the fMRI signal are also uniformly postulated to reflect the increased cerebral blood flow and eventual dilution of deoxy-hemoglobin (Hb) in the postcapillary part of the vasculature, with the additional effect of a local blood volume increase (Kim & Ress, 2016).

In efforts to improve the efficiency of fMRI, studies have revealed various systemic physiological components in BOLD signal fluctuations. Physiological parameters, such as cardiac pulsation (Chang *et al.*, 2009), blood pressure, and end-tidal carbon dioxide (CO_2) (Wise *et al.*, 2004; Murphy *et al.*, 2013), are considered artifact sources. The contamination is expected to be emphasized in resting-state fMRI (rs-fMRI), where signals are evaluated without trial averaging (Winder *et al.*, 2017). However, discrimination between neuronal and non-neuronal components has been a major challenge due to the lack of validation techniques with spatial and temporal precision comparable to that of fMRI. Another source of difficulty is the fact that many neural and non-neural parameters are intercorrelated in this low-frequency range (Murphy *et al.*, 2013).

A focus of recent studies exploring this matter is the spontaneous BOLD low-frequency oscillation (sLFO, < 0.1 Hz) possibly encompassing multiple artifact sources (Zhu *et al.*, 2015; Tong *et al.*, 2017). One well-known sLFO source is the respiratory volume fluctuation involving a chemoreflex loop (Birn *et al.*, 2008). An sLFO in systemic blood pressure, known as the Traube–Hering–Mayer wave, has been shown to originate from another autonomic loop (Guyton & Harris, 1951; Julien, 2006). Moreover, associated sLFOs in blood flow and velocity have been found (Killip, 1962; Fagrell *et al.*, 1977) and, later, transcranial Doppler ultrasonography and optical methods confirmed their traces

80 within the brain (Giller *et al.*, 1999; Obrig *et al.*, 2000). This optically detected sLFO was
81 found in both oxy- and deoxy-Hb with an interesting phase difference exclusively observed
82 in the brain (Rayshubskiy *et al.*, 2014; Tgavalekos *et al.*, 2016). Additionally, sLFOs were
83 found in electroencephalographic recordings, for which arterial vasomotion was suggested
84 as the origin (Nikulin *et al.*, 2014), although it is unclear how the vasomotion accounts for
85 the fMRI signal mainly from the capillary bed.

86 As mentioned above, Hb-sLFOs are postulated to be of systemic origin (Katura *et al.*,
87 2006; Tian *et al.*, 2011; Sassaroli *et al.*, 2012). Hence, it was not surprising to find a
88 correlation between the global fMRI signal and extra-cerebral signals (near-infrared
89 spectroscopy [NIRS] or MRI), but the constant time shift across body/brain parts was
90 unexpected (Anderson *et al.*, 2011; Tong *et al.*, 2012). The similarity between the low-
91 frequency phase map and perfusion MRI in healthy participants was a milestone in this
92 direction, as it presented the perfusion time lag embedded in the BOLD signal (Tong *et al.*,
93 2017). The resilient nature of the lag map against the fMRI task condition was shown,
94 further supporting its non-neuronal origin (Aso *et al.*, 2017*a*). In parallel, a number of
95 clinical studies have established the phase delays as a marker of cerebrovascular disorders
96 (Amemiya *et al.*, 2013; Lv *et al.*, 2013; Christen *et al.*, 2015; Ni *et al.*, 2017; Nishida *et al.*,
97 2018; Khalil *et al.*, 2018). Moreover, gross vascular anatomy has been detected consistently
98 in these studies, replicating the results from respiratory challenges (Chang & Glover,
99 2009*a*; Blockley *et al.*, 2011), which importantly suggests an equivalence between the
100 sLFO and manipulated circulatory turbulences. Apart from patient data, a recent study
101 involving healthy participants revealed changes in venous drainage patterns with normal
102 aging (Satow *et al.*, 2017). A body of evidence thus empirically supports the biological
103 significance of the low-frequency lag structure and its underlying principles.

104 The current analytical model of the BOLD lag structure assumes the presence of this
105 signal variation from the very early stages of cerebral perfusion (Tong *et al.*, 2018) (**Fig.**
106 **1A**). Such synchronized variation should naturally affect the global mean signal, and the
107 model is hence related to the unresolved fMRI global signal problem (Liu *et al.*, 2017;
108 Power *et al.*, 2017). This view is not only compatible with the occasional favorable effect

109 of global signal regression (GSR) in task fMRI (Aguirre *et al.*, 1998) but has led some
110 scientists to propose the removal of the lag structure as an approach for noise elimination
111 (Erdoğan *et al.*, 2016; Amemiya *et al.*, 2016; Byrge & Kennedy, 2018). Under this model,
112 the elimination of the lag structure can be viewed as an optimized GSR (of the low-
113 frequency component) for each voxel group. Conversely, with the presence of the BOLD
114 lag structure, a simple GSR should retain a residual correlation between in-phase voxels
115 that confounds fMRI analyses (Taylor Webb *et al.*, 2013; Erdoğan *et al.*, 2016).

116 The fundamental and critical question remaining is the mechanism by which sLFOs
117 (or respiratory maneuvers) create the BOLD lag structure. The BOLD response to neural
118 activity via NVC is a well-documented passive process, involving the expansion of the
119 intravascular compartment (Herman *et al.*, 2009). A typical model of the BOLD signal
120 change is described as follows (Hoge *et al.*, 1999):

121 $$\frac{\Delta BOLD}{BOLD_0} = M\left(1 - \left(\frac{CMRO_2}{CMRO_2|_0}\right)^{\beta}\left(\frac{CBV}{CBV_0}\right)\left(\frac{CBF}{CBF_0}\right)^{-\beta}\right) \qquad [1],$$

122 where $CMRO_2$ stands for the cerebral metabolic rate of oxygen in a voxel and CBV/CBF
123 represents the cerebral blood volume and flow, respectively. Beta (β) is an exponent of the
124 power-law describing the relationship between T2* and the deoxy-Hb amount that only
125 depends on $CMRO_2$ and CBF in a reciprocal manner, under the assumption of a negligible
126 inflow of deoxy-Hb. M is the factor for the BOLD susceptibility effect, defined as:

127 $$M \equiv TE \cdot B_0 \cdot CBV_0 \cdot [deoxy\text{-}Hb]_{V0}^{\beta} \qquad [2],$$

128 where B_0 is the main magnetic field strength and TE represents the echo time. Triggered by
129 vasodilation of the arteriole, this effect is diminished by an inflow of fresh blood, which
130 increases the MR signal. This baseline BOLD effect has been modeled in the formula for
131 the off-resonance frequency shift (δω) as follows (Yablonskiy & Haacke, 1994; An & Lin,
132 2002):

133 $$\delta\omega = \gamma \cdot \frac{4}{3} \cdot \pi \cdot \Delta\chi_0 \cdot Hct \cdot OEF \cdot B_0 \qquad [3],$$

134 where γ is the gyromagnetic ratio (42.58 MHz/T), $\Delta\chi_0$ is the susceptibility difference
135 between the fully oxygenated and fully deoxygenated blood, and Hct is the hematocrit

136 (volume fraction of erythrocytes to the blood volume, typically around 40%). The oxygen
137 extraction fraction (OEF) represents the only source of deoxy-Hb under the assumption of
138 100% oxygen saturation (SaO_2) in the inflow.

139 Variations of this base susceptibility can occur due to the local Hct and SaO_2 changes
140 and, in fact, have been shown to cause intersession variabilities (Cohen *et al.*, 2002;
141 Tuunanen & Kauppinen, 2006); however, within-session fluctuations have rarely been
142 considered (Thomas *et al.*, 2000). For example, even at a constant Hb density and oxygen
143 partial pressure, CO_2 fluctuation, a driving factor of vasomotion, alone can modify SaO_2
144 through pH changes (Collins et al., 2015a). Although the assumption of constant base
145 deoxy-Hb concentration may be sufficient for modeling its dilution by NVC (Ogawa *et al.*,
146 1998), other effects might not be negligible in non-neuronal fluctuations (**Fig. 1b**).

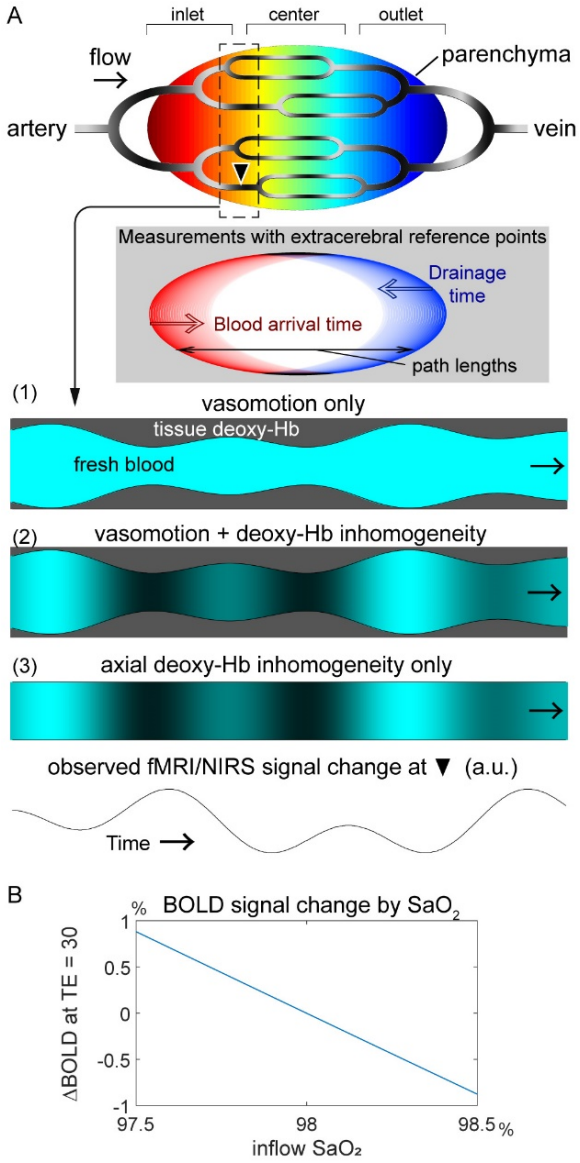

Fig. 1. A working model of BOLD lag mapping. (A) A schematic of the cerebral vascular tree presenting possible physiological models that account for the fMRI and NIRS observations. Each brain voxel has its lag (phase) of the spontaneous low frequency oscillation (sLFO) relative to the reference point, depicted in warm and cool colors. The inlet, center, and outlet parts of the gross vasculature are determined purely by the temporal relationship and not by vessel types; all signals should originate from the capillary bed. Another schematic is inserted to illustrate the effect of the reference point selection in relation to the vascular path length, which accounts for the disagreement with other blood-tracking techniques. Below are 3 models with different physiological signal sources that are moving along the vasculature. The current model with constant deoxy-Hb requires vasomotion to account for the sLFO (1). While the axial inhomogeneity of the deoxy-Hb density may be linked with vasomotion (2), it can persist without it (3). The moving axial inhomogeneity creates a similar temporal profile with varying phases across regions. (B) Dependence of the BOLD signal on inflow oxygen saturation (SaO_2) is a major determinant of the deoxy-Hb concentration at 3 T, TE = 30 ms. All other parameters were held constant at physiological values: oxygen extraction fraction = 45%, tissue blood volume fraction = 3%, and hematocrit = 40% (see Eqs. [1] and [2]).

BOLD, blood oxygen level-dependent; fMRI, functional magnetic resonance imaging; NIRS, near-infrared spectroscopy; TE, echo time; Hb, hemoglobin

179

180 In this exploratory study, we conducted 3 investigations to further advance our
181 knowledge on the BOLD lag structure and its underlying physiology. We first evaluated if
182 changes in blood transit velocity are embedded in the BOLD low-frequency phase to
183 confirm its behavior as a virtual tracer [a preliminary analysis of these data was presented
184 previously as a poster (Aso *et al.*, 2017*b*)]. Next, we investigated the effect of eliminating
185 the lag structure from task-based fMRI, which had not been tested previously. Finally, we
186 used multi-echo imaging to assess the components of the BOLD signal that determine the
187 lag structure. One of the recent approaches toward fMRI denoising has focused on S_0
188 fluctuations (signal at TE = 0, which is the baseline MR signal from the fluid
189 compartments), as it is weakly associated with neural activity (Posse *et al.*, 1999; Wu *et al.*,
190 2012; Kundu *et al.*, 2012; Yen *et al.*, 2017). In contrast, the total-Hb sLFO, detected by
191 NIRS, is interpreted as a local CBV change under the assumption of a constant Hct, which
192 should also affect the non-BOLD component via changes in plasma volume and inflow
193 (Rostrup *et al.*, 2005). Notably, the contributions of the T2* and S_0 components may differ
194 from NVC contributions to the BOLD lag structure; hence their impact may have been
195 overlooked in studies based on trial averaging. From the influences of 3 different fMRI task
196 paradigms, including a simple reaction-time visuomotor task, a short breath-holding task,
197 and a hyperventilation task on the neural and non-neural components of the fMRI signal,
198 we sought further validation of our hypothetical model of the BOLD lag structure.

199 **2 Materials and methods**

200 **2.1 Participants and experimental procedures**

201 Twenty-one healthy participants (8 women, 19–26 years of age) participated in Experiment
202 1; only 1 person was excluded from the analysis because of an abrupt head motion, which
203 prevented BOLD lag mapping (see Data processing). The remaining 20 participants
204 performed the sparse visuomotor and 10-s breath-holding tasks, but the hyperventilation
205 task was only performed by 18 participants, as it was introduced after the first 2 individuals
206 had concluded their participation. Another 21 participants were recruited for Experiment 2,

involving multi-echo acquisition, all of whom performed the above 3 tasks but with an 18-s version of the breath-holding task. To avoid vigilance level fluctuations, all MRI sessions were scheduled in the morning and the participants were encouraged to sleep well the previous night.

The protocol for this study was approved by the internal ethics review board of Kyoto university. The participants provided written informed consent in advance, according to the Declaration of Helsinki, for the analysis of anonymized MRI scans and simultaneously acquired physiological data.

2.2 Image acquisition

A Tim-Trio 3-Tesla scanner (Siemens, Erlangen, Germany) with a 32-channel phased-array head coil was used for MRI acquisition. For Experiment 1, T2*-weighted echo-planar images were acquired using multiband gradient-echo echo-planar imaging (EPI) (Feinberg *et al.*, 2010) with the following parameters to cover the entire cerebrum: 64 × 64 pixels, 35-slice interleave , 192-mm field of view (FOV), 3.5-mm slice thickness, repetition time (TR)/ TE = 500/35 ms, flip angle = 40°, and a multiband factor of 5. Three 9-min runs (1,080 volumes) were acquired for each of the 3 task conditions. The same pulse sequence program was used in Experiment 2 but with multi-echo settings: TE1 = 7.76 ms and TE2 = 25.82 ms for the first 6 participants and TE1 = 11.2 ms and TE2 = 32.78 ms for the remaining 15 participants. A smaller multiband factor of 2 was selected to allow for the short TE in combination with parallel imaging using GeneRalized Autocalibrating Partial Parallel Acquisition. Other acquisition parameters were: TR = 1,300 ms, flip angle = 65°; 36-slice interleave, FOV = 256 × 192 mm^2, 64 × 48 matrix, and 3.5-mm slice thickness. Three 7-min (323 TR) runs were acquired. Seven participants in Experiment 2 underwent 2 additional runs with a shorter TR of 700 ms and a flip angle of 45° to examine the sensitivity of the respiration-related signal component to inflow modulation. At the end of every experimental session, a 3-dimensional (3D) magnetization-prepared rapid acquisition with gradient echo (MPRAGE) T1-weighted image was acquired for obtaining anatomical information (Aso *et al.*, 2017*a*). A dual-echo gradient-echo dataset for B_0 field mapping was also acquired after the BOLD scan in the same orientation.

236 **2.3 Task conditions**

237 Throughout the experimental session, task instructions were presented via a liquid crystal
238 display (LCD) monitor inside the scanner room, viewed through a mirror. Beat-to-beat
239 fluctuations in the mean arterial pressure and heart rate were obtained via a non-invasive
240 MR-compatible device (Caretaker, BIOPAC Systems, Inc., Goleta, CA, USA). Careful
241 instructions were provided to the participants on how to avoid motion, especially during the
242 respiratory challenges.

243 **2.3.1 Sparse visuomotor task**

244 A simple visuomotor task with a varying intertrial interval of 6 to 24 s was performed
245 during the first run. Participants were instructed to press a button with their right index
246 finger as soon as the computer screen changed from "Please hold still" to "Press the
247 button." The screen returned to "Please hold still" at the button press or after 3 s, if the
248 participant had not pressed the button.

249 **2.3.2 Breath-holding task**

250 To minimize head motion induced by the tasks, the 2 respiratory challenges were adapted
251 to be less strenuous than in earlier studies. In Experiment 1, the breath-holding task was
252 cued by a "Hold your breath" instruction on the screen, at which point the participants were
253 asked to immediately hold their breath, irrespective of the respiration phase. The holding
254 periods lasted 10 s and were separated by 90-s intervals. This short duration was selected to
255 minimize strain that can cause body movements, while evoking a detectable autoregulatory
256 response (Murphy *et al.*, 2011). In Experiment 2, a longer holding period of 18 s after a
257 brief inhalation for 2 s was used to evoke a more pronounced vasodilation.

258 **2.3.3 Hyperventilation task**

259 The hyperventilation task involved paced breathing at 0.2 Hz for 25 s, separated by a 30-s
260 rest. Each 5-s cycle began with the screen presenting "Please inhale" for 1.5 s, followed by
261 "Please exhale slowly," lasting 3.5 s. Participants were instructed to breathe as deeply as
262 possible, while avoiding head movement. A short inspiration period was selected to
263 suppress motion by minimizing movements in the thoracic cage and spine.

264 **2.4 Data processing**

265 For image processing, SPM12 (Wellcome Department of Cognitive Neurology, London,
266 United Kingdom) and FSL5 (FMRIB Software Library, www.fmrib.ox.ac.uk/fsl) (Smith *et*
267 *al.*, 2004) were used in combination with in-house MATLAB scripts. Off-resonance
268 geometric distortions in the EPI data were corrected using FUGUE/FSL with B_0 field maps.
269 After inter-scan slice-timing correction, head motion was compensated by 3D motion
270 correction and data repair (Mazaika *et al.*, 2009). The repairing procedure aimed to remove
271 motion-related signal dropout and involved searching for time points satisfying 2 stringent
272 criteria: (1) global signal changes between consecutive volumes exceeding 1% and (2) head
273 displacement exceeding a Euclidian distance of ± 1 mm or ± 1° rotation per TR. The
274 affected time points were replaced with linearly interpolated values, but this procedure was
275 required in only 6 of the 41 participants.

276 The data were further cleaned by regressing out 24 head motion-related parameters.
277 Unlike in previous studies, the 6 rigid-body parameter time series were not directly used
278 because of the possible contamination of the motion parameters with the global signal when
279 the participants were immobile (Freire & Mangin, 2001). We used the first temporal
280 derivatives of the motion parameters, their versions after being shifted by 1 TR, and the
281 squares of those 12 time series (Satterthwaite *et al.*, 2013). Images were spatially
282 normalized to the template space using the T1-weighted anatomical image and resliced to a
283 4-mm isotropic voxel size to achieve a high voxel temporal signal-to-noise ratio.

284 **2.4.1 Lag mapping**

285 A recursive technique was used (Aso *et al.*, 2017*a*) after temporal bandpass filtering at
286 0.008–0.07 Hz to ensure that the phase was uniquely determined within the cross-
287 correlation range. Whereas lag was tracked up to 7 s for most analyses, it was limited to 4 s
288 in both directions, upstream and downstream, for the calculation of the relative BOLD
289 transit time (rBTT, see below). This shorter tracking range allowed a higher cutoff
290 frequency (0.12 Hz) to preserve the high-frequency component in the velocity change
291 profiles.

The global mean signal was used to select the initial seed that defined the reference phase (lag = 0). First, voxels presenting a cross-correlogram peak at 0 with the global signal were determined. The time course averaged over this set of voxels served as the initial reference. In each step of the recursive procedure toward up- and downstream, a cross-correlogram was calculated between the time series obtained from the previous seed voxels and every undetermined voxel to find a set of voxels with a peak at ± 0.5 s, which then served as the new seed. This tracking part retained some voxels without any lag values because cross-correlogram peaks < 0.3 were not used following earlier works (Tong et al., 2017). These voxels were later filled 1 by 1 with average phases from voxels with similar time courses and correlation coefficients > 0.3. There were single isolated holes even after this procedure, which were filled by linear interpolation, using the 6 neighbors. There is a concern that this correlation coefficient threshold is too low to accurately claim a significant correlation. However, recursive tracking involves finding the cross-correlogram peak precisely at ± 0.5 s, which conveys different information from its height. Besides, most earlier works empirically supporting the biological significance of this phenomenon involved no thresholding. When the threshold correlation coefficient was increased to 0.6, most brain voxels required the hole-filling procedure, but we still obtained lag maps (by between-voxel intra-class correlation (2,1) > 0.4) in 16 out of 20 participants during resting state and 17 during 10-s breath holding.

2.4.2 fMRI analysis on "cleaned" BOLD datasets

Individual BOLD data from Experiment 1, after the above pre-processing steps including the motion parameter regression, served as the reference or "raw" dataset. GSR with a low-pass filtered global signal, a normal GSR, global scaling implemented in SPM12, and without the perfusion lag structure ("deperfusioned") were compared with the raw dataset.

The GSR involves regression by the global signal and extracting the residuals in each voxel. In deperfusioning, instead of the uniform regressor, a corresponding time series was used for each voxel group by the lag value ("dynamic" GSR) (Erdoğan *et al.*, 2016). For global scaling, the raw dataset was entered into the same SPM pipeline, except for the option of internally dividing each volume by its global mean signal instead of the constant

321 session mean. The normal GSR and global scaling thus affected all frequency ranges,
322 whereas the GSR and deperfusioning removed only the low-frequency components.

323 Random effects analysis (Friston *et al.*, 2002) was used to evaluate the effect of these
324 procedures on the fMRI results from the standard analysis framework. For the visuomotor
325 task, the neural response to each trial was modeled as an event of 0.5 s in duration. For the
326 hyperventilation condition, a boxcar with a 25-s duration modeled the activation related to
327 volitional respiratory control. Similarly, both the onset and offset timing of breath holding
328 were used to model the time-locked neural activity. The canonical hemodynamic response
329 function was convolved to the model time series to create the regressors of interest. The
330 threshold for all activation maps was $p = 0.05$ after correcting for multiple comparisons,
331 using family-wise error across the whole brain (Poline *et al.*, 1997).

332 **2.4.3 Relative BOLD transit time**

333 **Fig. 3A** illustrates the method. This analysis was performed on data from Experiment 1,
334 acquired at a short TR of 0.5 s. The lag structure consisted of a lag map and the set of time
335 series averaged over the voxels with the same phase. This structure represents the
336 propagation of the sLFO phase along the vessels. The phase is expected to move across
337 adjacent regions of the vascular tree every 0.5 s, the lag tracking step, on average.
338 However, if there is variation in propagation velocity, there would be a deviation of the
339 instantaneous phase difference from 0.5. Here, the phase difference is supposed to reflect
340 the time the blood requires to cross the boundary between the neighboring voxel groups.

341 Based on this supposition, the phase difference fluctuation was calculated from each
342 of the 16 pairs of seeds corresponding to lags of -4 to +4 s at 0.5-s intervals. Due to the
343 broad frequency range of the fluctuations of interest, we chose a smooth sliding window
344 algorithm (window length = 30 s, Kaiser window with a β value of 4) instead of using
345 analytic methods (e.g., Hilbert transform). The region time series were resampled to a 0.02-
346 s resolution to capture minute phase difference fluctuations (4%) from 0.5 s. Instantaneous
347 phase differences from each pair of seeds were averaged over respiratory task events and
348 divided by 0.5 to obtain the time course of the rBTT. The rBTTs from the 16 pairs of
349 neighboring regions were then averaged to obtain the regional or global rBTT. According

350 to this model, the inverse of the rBTT corresponded to the instantaneous velocity (relative
351 to the baseline average velocity), as the rBTT should reflect the average time required to
352 traverse fixed distances.

353 **2.4.4 Multi-echo combination**

354 For Experiment 2, involving multi-echo acquisition, S_0 and T2* datasets were created by a
355 simple estimation used in earlier works (Posse *et al.*, 1999; Yen *et al.*, 2017). We assumed
356 a single compartment monoexponential decay of the MR signal as follows:

357

358 $$\boldsymbol{S(TE) = S_0\ exp(-TE/T_2{}^*)} \quad [4],$$

359

360 where T2* and S_0 were calculated for each TR as follows (Kundu et al., 2012; Posse et al.,
361 1999):

362

363 $$\boldsymbol{T2^* = (TE2 - TE1)/\ln(S_1/S_2)} \qquad [5], \text{ and}$$

364

365 $$\boldsymbol{S_0 = S_1{}^{TE2/(TE2-TE1)}/S_2{}^{TE1/(TE2-TE1)}} \qquad [6],$$

366

367 where S_1 and S_2 are the acquired signals at TE1 and TE2, respectively. Negative or T2*
368 values exceeding 100 ms were considered as noise and were ignored. All four datasets (S_0,
369 S_1, S_2 or BOLD, and T2*) were entered into the same analysis pipeline used for Experiment
370 1 while accounting for the different TR value of 1.3 s. The following analyses were
371 performed on a resampled time course with a TR of 0.5 s.

372 The interaction between the signal component and vascular anatomy was examined
373 by extracting the signal time series from the inlet, center, and outlet parts of the vascular
374 tree, based on the individual lag map created from the BOLD (i.e., at TE2) dataset. By
375 exploiting the longer lag tracking range (± 7 s) than the one used in the rBTT analysis in

Experiment 1, the center region in this analysis covered a wider range (± 2.5 s). Using the JMP12 software (SAS Institute, Cary, NC), the magnitude and phase of the regional signals were analyzed by repeated-measures ANOVA followed by post hoc analyses, using Tukey's honestly significant difference (HSD) test. Statistical significance was set at $p < 0.05$. Additional analyses were performed to examine the origins of the signal components, including a region-of-interest analysis and an SPM analysis of respiration phase-related small S_0 fluctuations.

3 Results

The average root mean square of the head motion was measured as the framewise displacement (i.e., the shift in the position of the brain in 1 volume compared to the previous volume), was 0.039 ± 0.007 mm (mean ± standard deviation (SD) over participants) for Experiment 1, with a maximum displacement of 0.37 ± 0.18 mm, and 0.034 ± 0.015 mm for Experiment 2, with a maximum of 0.24 ± 0.12 mm (Van Dijk et al., 2012).

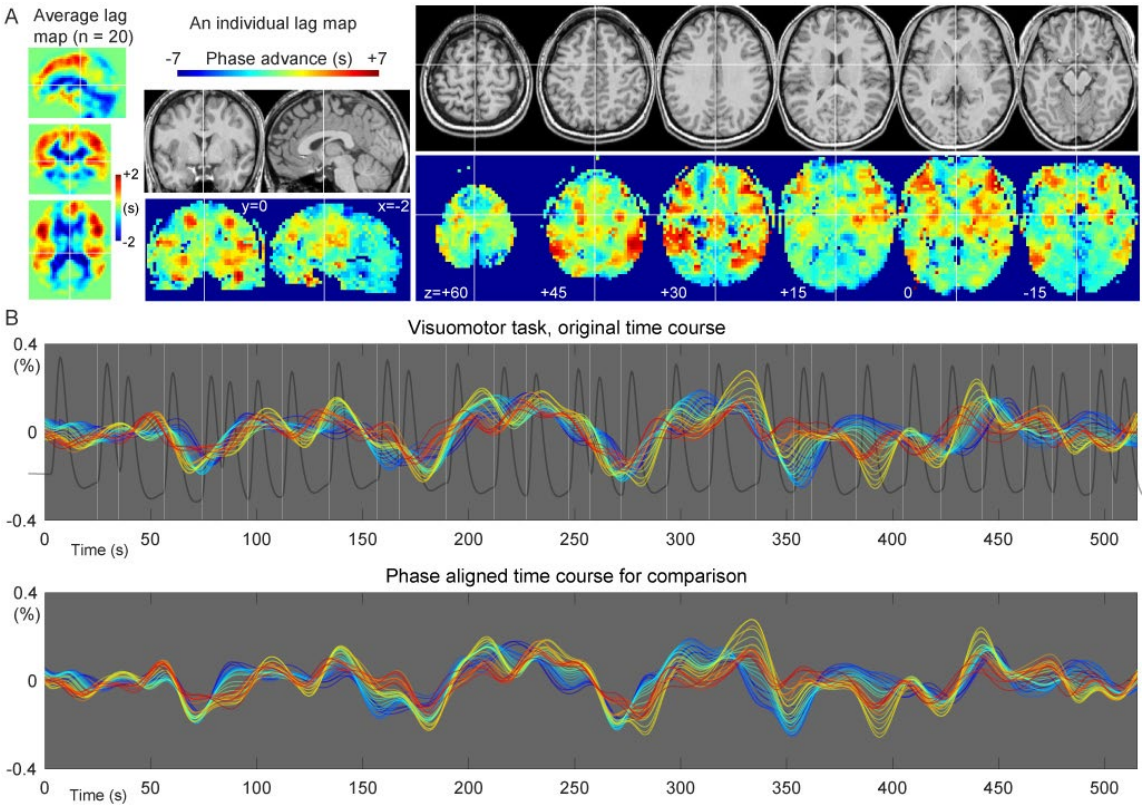

Fig. 2. Representative spatial and temporal profiles of the BOLD lag structure. (A) A lag map created by tracking the BOLD sLFO phase up to 7 s toward both up- and downstream is shown. The group average map shows the gross vascular anatomy with the early phase (positive values) distributed in the middle cerebral artery territories. The individual map provides more detailed information. (B) Seed time courses updated at each step (0.5 s) of the recursive lag tracking procedure, representing the temporal aspect of the lag structure, are shown. The warm-colored traces with advanced phases originate from the voxels with the same colors in the lag map, corresponding to the inlet or arterial side of the vasculature. A gradual change in the temporal profile is noted on top of the slow component, which is stable across regions. The white vertical lines indicate the timing of the visuomotor task, whose NVC was modeled by the hemodynamic response function (dark gray trace). The detected LFO was poorly correlated with the task-related fluctuation of neuronal origin (see main text).

BOLD, blood oxygen level-dependent; NVC, neurovascular coupling

Fig. 2A shows an individual and the average BOLD lag maps during the sparse visuomotor task. Warm colors indicate a positive travel time from those voxels to the phase of the global LFO, signifying that the voxels are considered "upstream." Most brain voxels fell into the -4 to +4 s range (mean ± SD, 93.8 ± 2.9%). The recursively defined seed time courses are shown in **Fig. 2B** with warm colors indicating averaged time series from the upstream voxels. This time course of the lag structure was poorly correlated with the visuomotor task (white vertical lines) or the evoked NVC response (trace in dark gray), supporting a non-neuronal origin of the sLFO. This was confirmed by the correlation coefficient between the global mean signal and the modeled response that was not significantly different from 0 (0.0265 ± 0.140, mean and SD over 20 participants), although still slightly positive in some participants and its regression affected the activation maps (see section 3.2). In addition to the constant phase shift across regions, the lag structure time courses presented minute fluctuations of the phase difference (i.e., the temporal relationship between the lines) over time.

3.1 Flow velocity information in the instantaneous phase

A transient change in the propagation velocity of the low-frequency phase, obtained as the inverse of the global rBTT, was found in response to the respiratory challenges. **Fig. 3B** shows the stacked histograms of the distribution of the instantaneous phase difference measured by the moving window analysis. This instantaneous phase difference is interpreted as the time the blood takes to move over a unit distance that requires 0.5 s on average. The time courses are presented in **Fig. 3C**. After approximately 10 s of delay, an increase and a decrease of the BOLD signal was found during breath holding and hyperventilation, respectively (arrows).

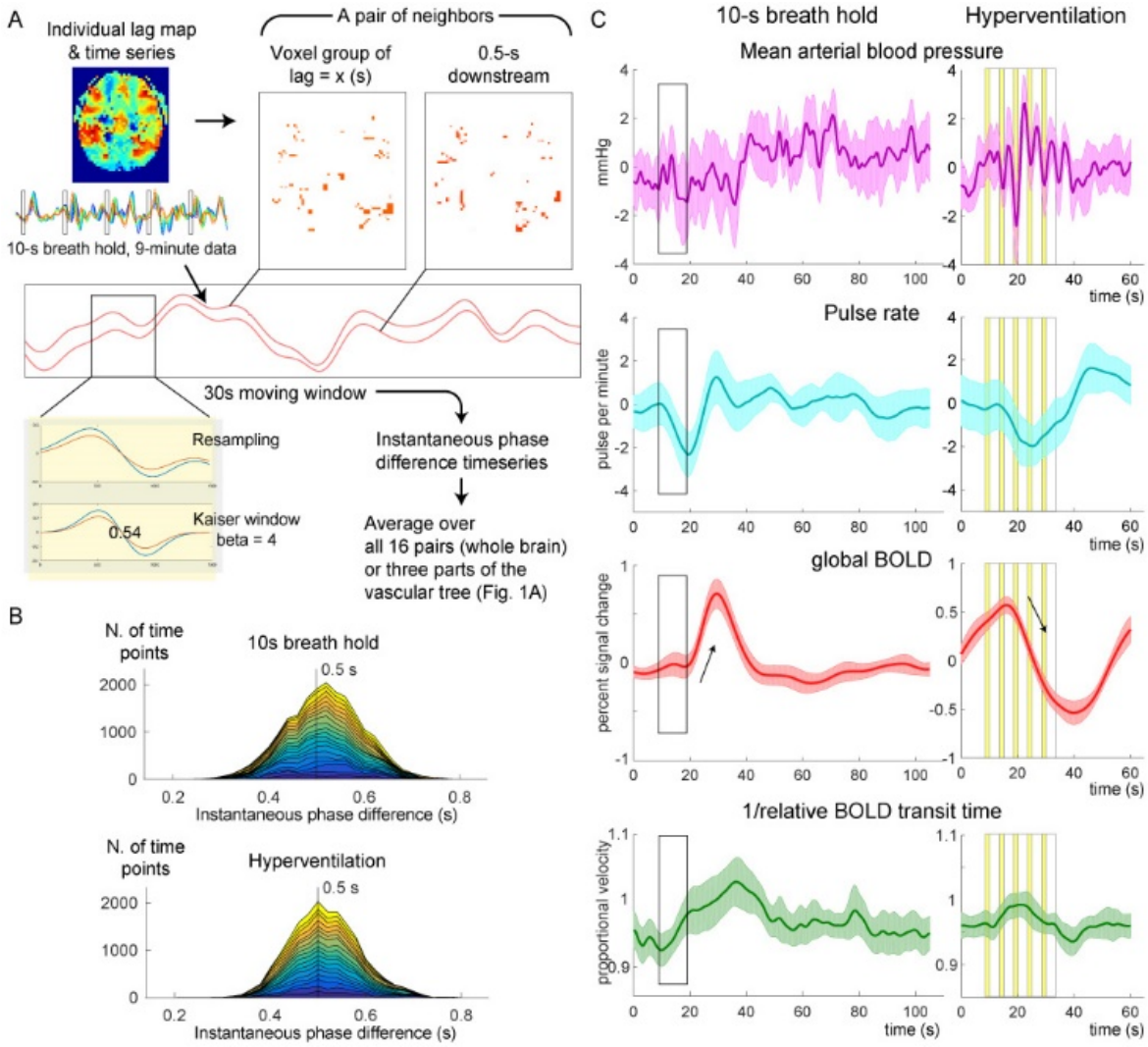

431 **Fig. 3.** Measurements of the relative BOLD transit time (rBTT). (A) A schematic
432 illustration of the analysis is presented. For each pair of voxel groups representing
433 neighboring regions of the vascular tree, the 2 average time series were fed into a
434 moving window analysis of instantaneous phase difference. (B) Time point histograms
435 of the instantaneous phase difference averaged over 16 pairs of neighboring regions in
436 the lag structure are shown. Twenty participants are stacked. Deviation of the phase
437 difference from 0.5 s reflects a fluctuation of the flow velocity, although the slight shift
438 of the peak is observed in the breath hold data presumably due to windowing. (C)
439 Responses to the respiratory challenges of the physiological recordings, raw BOLD
440 signal, and inverse of the rBTT that can be interpreted as relative velocity are shown.
441 Thin arrows indicate the autoregulatory response of the raw BOLD signal. The 5
442 cycles of volitional breathing for hyperventilation are indicated with yellow bands
443 representing the inspiration phase. Shaded areas indicate the 95% confidence interval
444 of the mean across participants.

445 BOLD, blood oxygen level-dependent

446

447 The temporal profile of the instantaneous velocity (green curves) was roughly in
448 phase with the global BOLD response but had different onset and peak timings, indicating
449 different physiological bases. To evaluate the relationship of this phenomenon with the
450 vascular structure, the inlet, center, and outlet regions were separately analyzed (**Fig. 4**). In
451 both respiratory challenges, there was a clear asymmetry over the vasculature, with
452 pronounced velocity responses in the inlet region. Despite similar BOLD response profiles,
453 the velocity response was not clearly found in the outlet region.

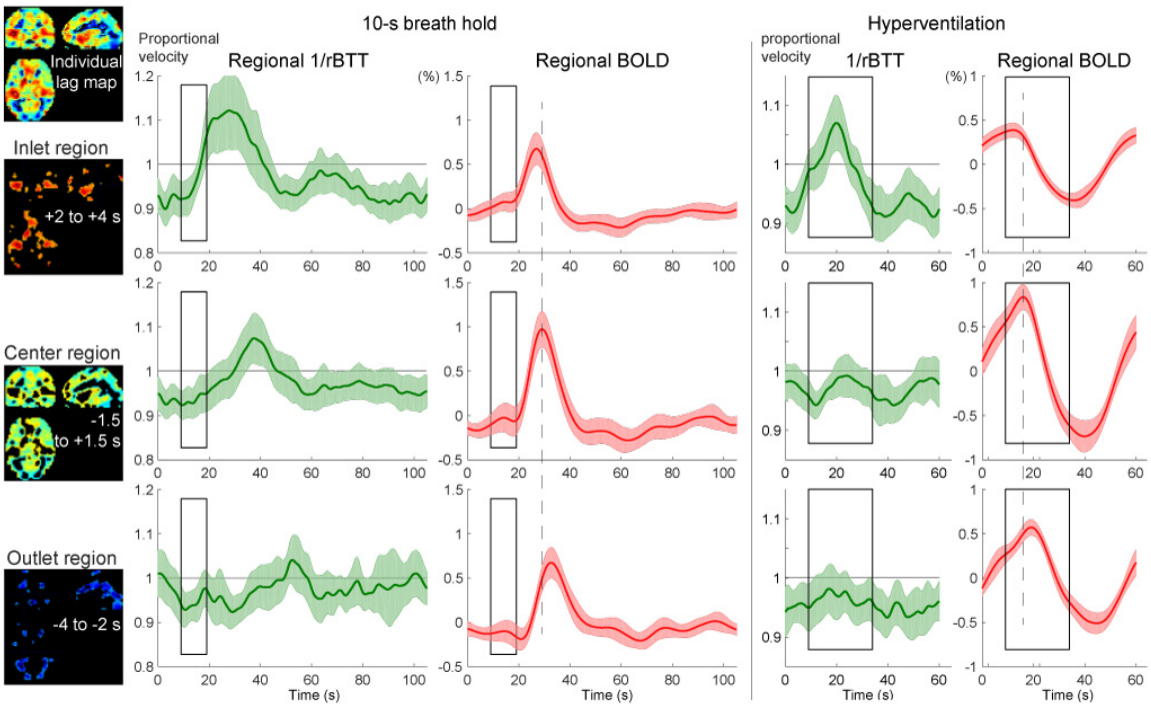

Fig. 4. Autoregulatory responses to respiratory challenges in the 3 vascular regions, using the same conventions as in **Fig. 3**. The inlet (arterial side), center, and outlet (venous side) of the parenchymal vasculature were defined for each participant, using the lag map created from the session data. The relative changes in propagation velocity were detected as the inverse of the instantaneous transit time deviation from 0.5 s (rBTT), since the lag mapping was performed in 0.5-s increments. The BOLD signal time courses present different peak latencies for the 3 regions (broken lines are aligned to the center region peak), directly reflecting the lag structure, but with similar profiles, ruling out its effects on the rBTT measurement. Shaded regions represent the 95% confidence intervals (N = 20).

BOLD, blood oxygen level-dependent

3.2 Effect of deperfusioning on the detection of neurovascular coupling

Removal of the whole lag structure exhibited unique effects on the fMRI analysis. While the mean and SD images from the individual activation maps showed similar spatial distributions, all procedures reduced the sensitivity compared to the raw dataset where only

the motion-related variances were removed (**Fig. 5**). However, after the deperfusioning procedure, primary motor cortex activation was successfully detected by decreased interindividual variances (black circles). The effect of these procedures was not uniform between the respiratory challenges (**Fig. 6**), but some interpretable clusters were selectively captured by the "deperfusioned" signals despite the reduced cluster number. For example, the laryngeal motor cortices were detected at the onset and offset of the 10-s breath-holding sessions (Kumar *et al.*, 2016). In the hyperventilation condition, bilateral recruitment of the putamen was noted. Additionally, a premotor peak was found at coordinates [+56, 0, 40].

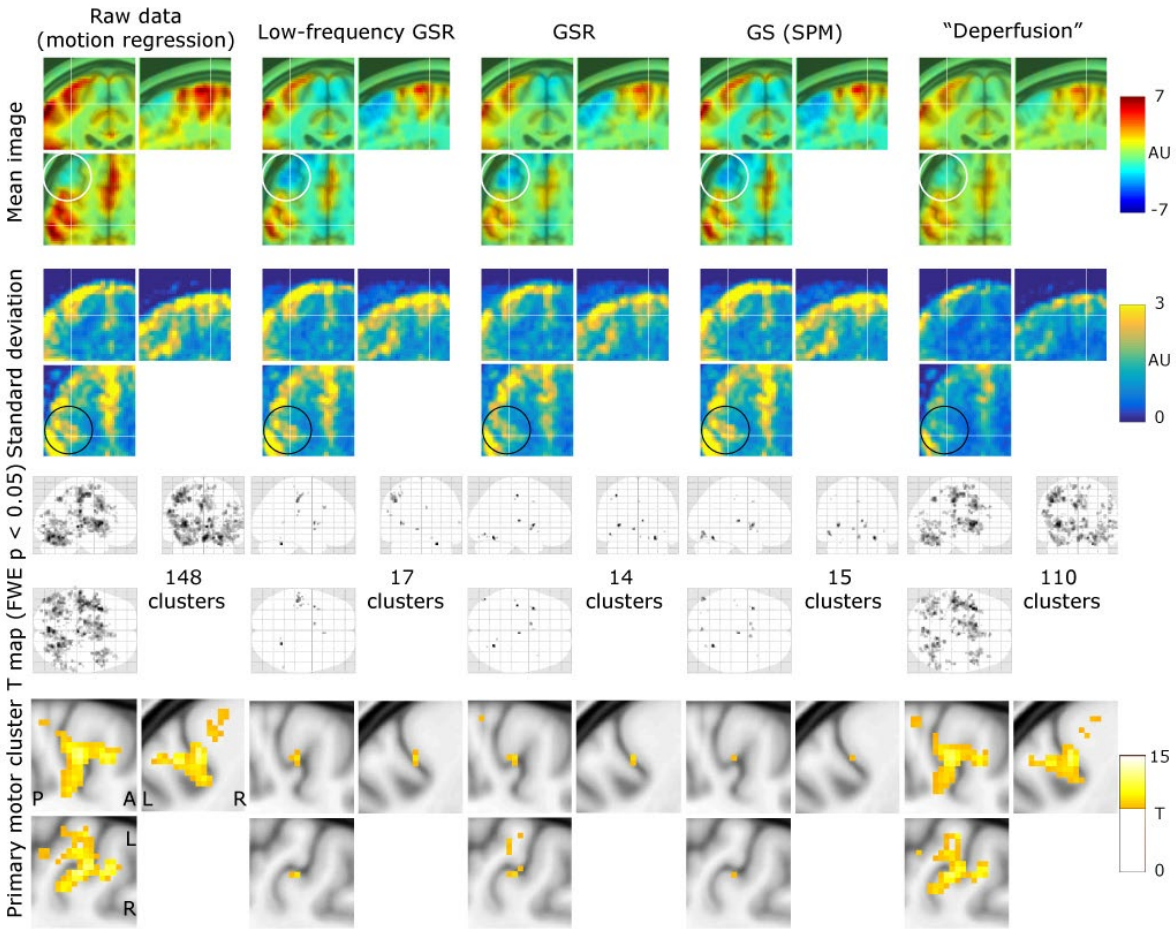

Fig. 5. The effects of the denoising procedures on the detection of neurovascular coupling during the visuomotor task. Mean and standard deviation maps from 20 individual activation maps (contrast images) illustrate the spurious negative responses by the global-signal based methods (white circle) and the reduced between-participant

variation by the lag structure removal or deperfusioning (black circle). The threshold for the activation maps was p = 0.05, corrected for FWE of multiple comparisons over the entire brain, and zoomed in to show the "hand-knob" of the left primary sensorimotor cortex.

FWE, family-wise error corrected; GSR, global signal regression; GS, global scaling; SPM, SPM12 software

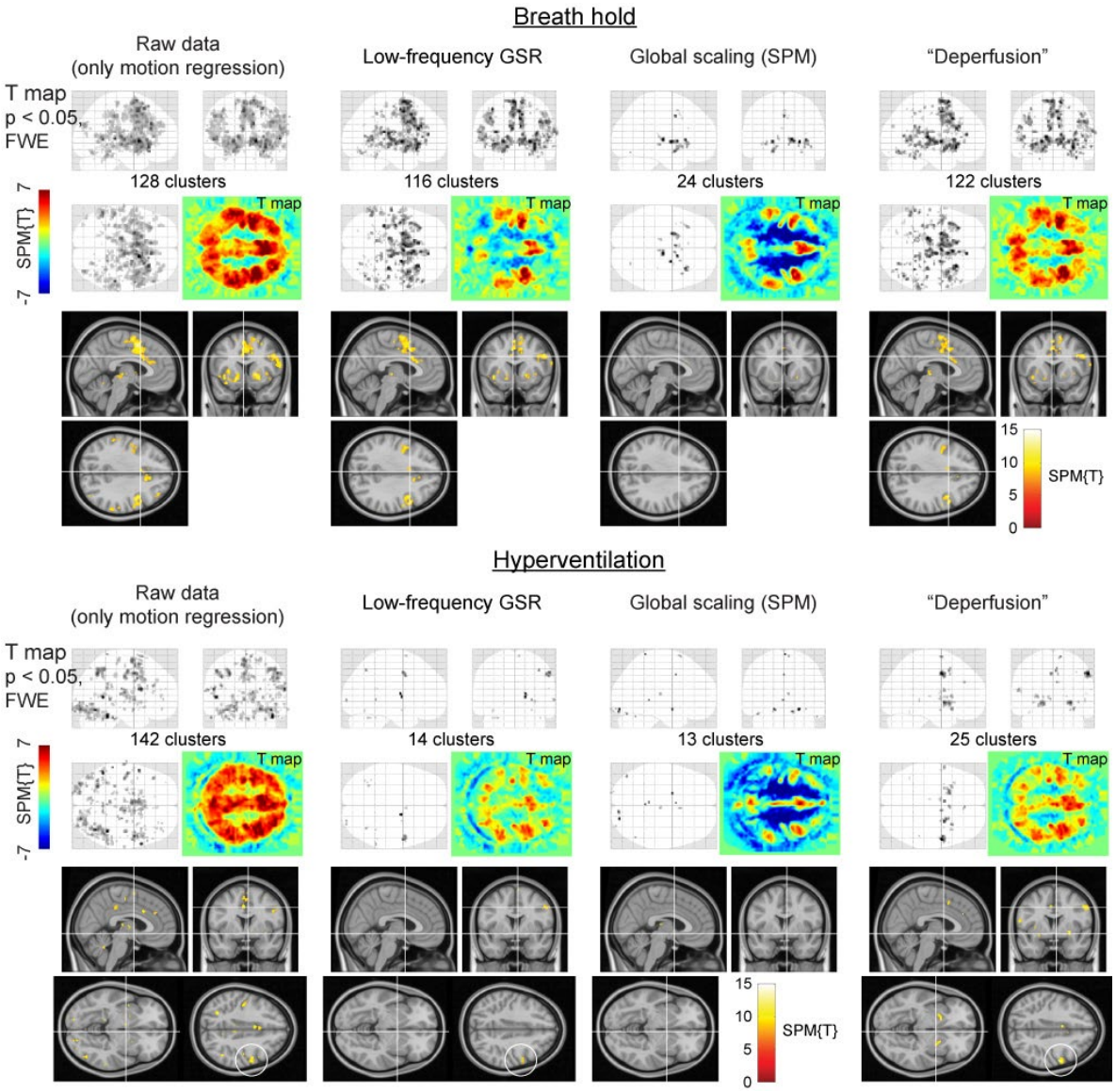

Fig. 6. SPM results of the respiratory challenges. Color panels show un-thresholded t map slices at the height of the laryngeal motor cortex (z = 35), revealing spurious

negative responses (cool colors) after global signal removal but not after the deperfusioning procedure. In the hyperventilation condition, the "deperfusioned" data revealed clusters in the bilateral putamen and premotor cortex (white circle), consistently with the findings of earlier reports.

FWE, family-wise error corrected; GSR, global signal regression; GS, global scaling; SPM, SPM12 software

Voxel histograms from the group SPM analyses showed clear leftward shifts by the global signal removal, indicating spurious deactivations (**Fig. 7**). The correlation of the neuronal response with the global signal (or the extracted sLFO) was near 0, as described above, but it varied across participants and tended to be positive. This trace of NVC may have created the spurious deactivation after regression. Notably, this effect was very weak after deperfusioning across all 3 conditions (green plots), despite a large amount of variance removed by the procedure.

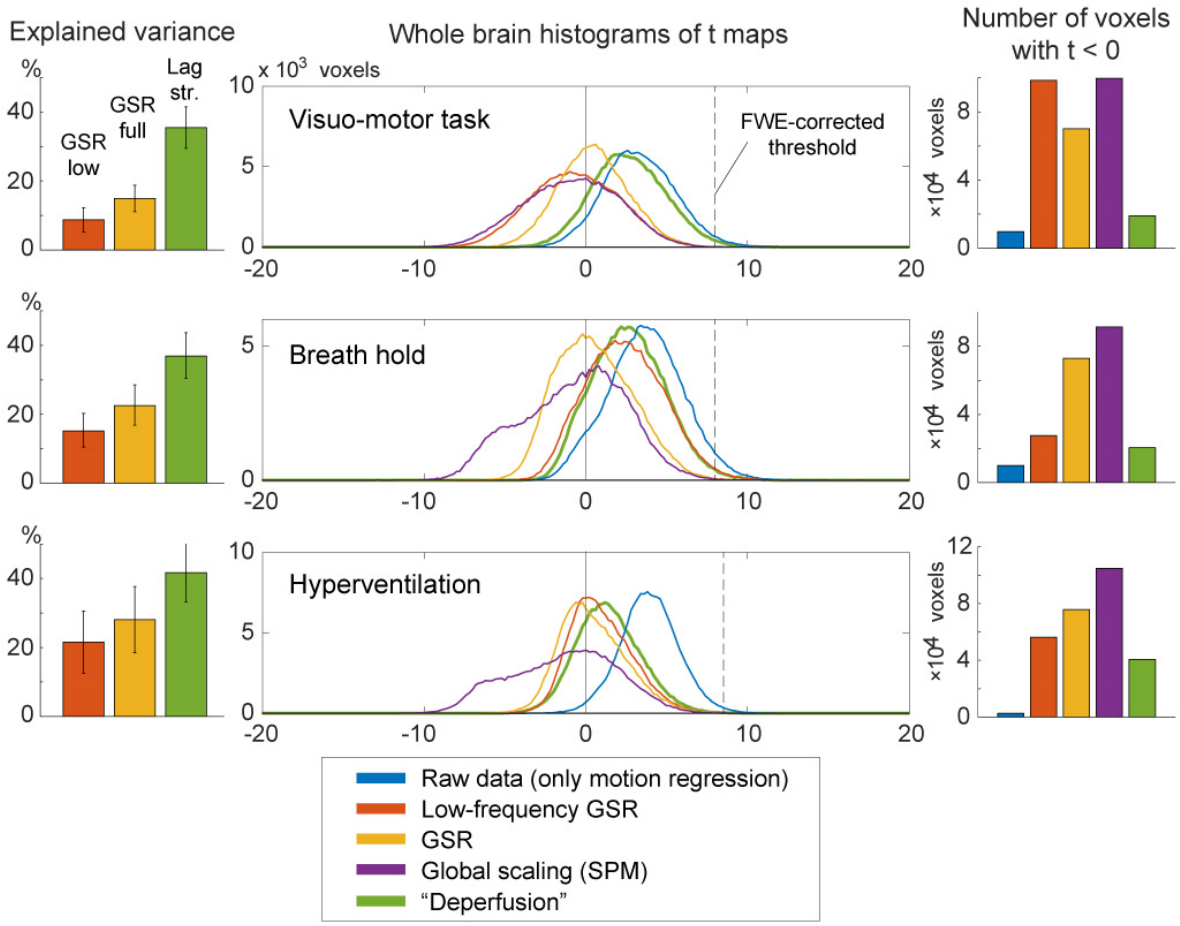

Fig. 7. The effects of preprocessing on group SPM analyses. Removal of the lag structure or deperfusioning resulted in the greatest reduction of the signal variance under all 3 tasks (left panels). Nevertheless, the spurious negative task responses were attenuated in comparison to the removal of global fluctuation (middle and right panels). Error bars indicate the standard deviation. The vertical broken line in the histogram indicates the statistical height threshold of p = 0.05, corrected for multiple comparisons by the family-wise error (FWE) rate.

GSR, global signal regression; SPM, SPM12 software

3.3 Magnetic resonance signal components of the lag structure

As depicted in **Fig. 8**, the percent signal change of the sLFO, or the lag structure amplitude, revealed a clear T2*-dependence with a significant reduction of amplitude in the outlet (i.e.,

520 the venous side of the gross vasculature [post hoc Tukey's HSD between T2* signals from
521 the inlet and outlet regions, following a repeated-measures ANOVA]).

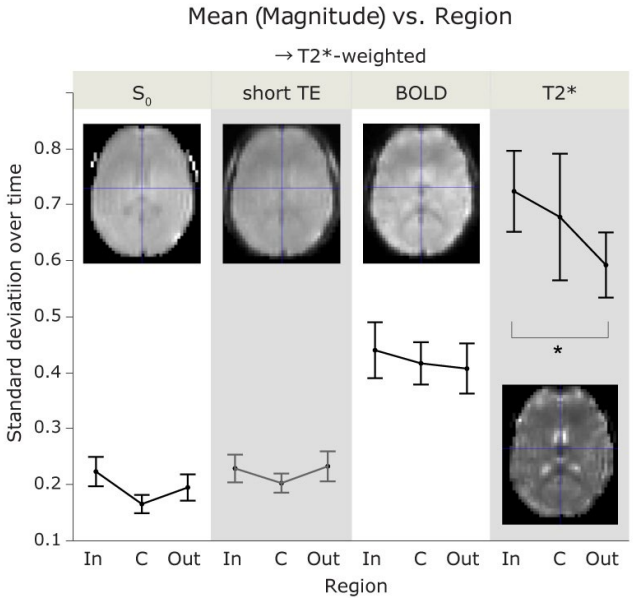

522

523 **Fig. 8.** The standard deviation of the percent signal change as a measure of sLFO
524 magnitude. No main effect of vascular region was observed by repeated-measures
525 ANOVA, but the T2* magnitude was significantly different between the inlet and
526 outlet sides ($p < 0.05$, Tukey HSD). The short-TE image was not included in the
527 ANOVA to avoid data redundancy. Each error bar is constructed using a 95%
528 confidence interval of the mean.

529 sLFO, spontaneous low-frequency oscillation; ANOVA, analysis of variance; TE, echo
530 time; In, inlet; C, center; Out, outlet

531

532 In lag maps from the 3 T2*-weighted images, there were some effects of the
533 respiratory challenges, but the gross cerebral vascular structure was preserved across tasks;
534 the periventricular regions and major venous sinuses were uniformly found downstream
535 (i.e., with negative arrival time) of the global signal phase, while the cortical territory of the
536 middle cerebral arteries exhibited earlier arrival (**Fig. 9A**). Only the S_0 image presented a
537 different lag structure, according to the image similarity (**Fig. 9A**, right panels).

538 Temporal analysis of the signal components revealed significant main effects of both
539 region [$F(2,532) = 16.877$, $p < 10^{-6}$] and T2* weighting [$F(2,532) = 280.786$, $p < 10^{-6}$]
540 (**Supp. Fig. 1A**). The S_0 time series failed to show a correlation with the T2*-weighted
541 signals, but the z-value in the inlet (i.e., the arterial side) differed significantly from that in
542 other regions ($p < 0.05$, Tukey's HSD). A region effect was also found for phase
543 relationships (**Supp. Fig. 1B**). Similarly, the main effects for both region [$F(2,532) =$
544 27.548, $p < 10^{-6}$] and T2* weighting [$F(2,532) = 44.679$, $p < 10^{-6}$], as well as their
545 interaction [$F(4,532) = 24.902$, $p < 10^{-6}$], were significant. The phase of the TE1 signal,
546 which is less T2*-weighted than that of the BOLD signal, gradually advanced, finally
547 showing a phase lead in the outlet region, further supporting an interaction between the
548 signal components and vascular regions. These signal phase dissociations within regions
549 are displayed in **Supp. Fig. 1C**. Significant differences among the 3 T2*-weighted signals
550 were also found after the post-hoc test ($p < 0.05$). The signal-region interaction was evident
551 in the signal response to the respiratory challenges shown in **Fig. 9B**. Note that the traces
552 contain higher frequency components that were eliminated prior to lag mapping. In contrast
553 to the changes in T2* responses for both phase and magnitude, the S_0 component was
554 stable across vascular regions.

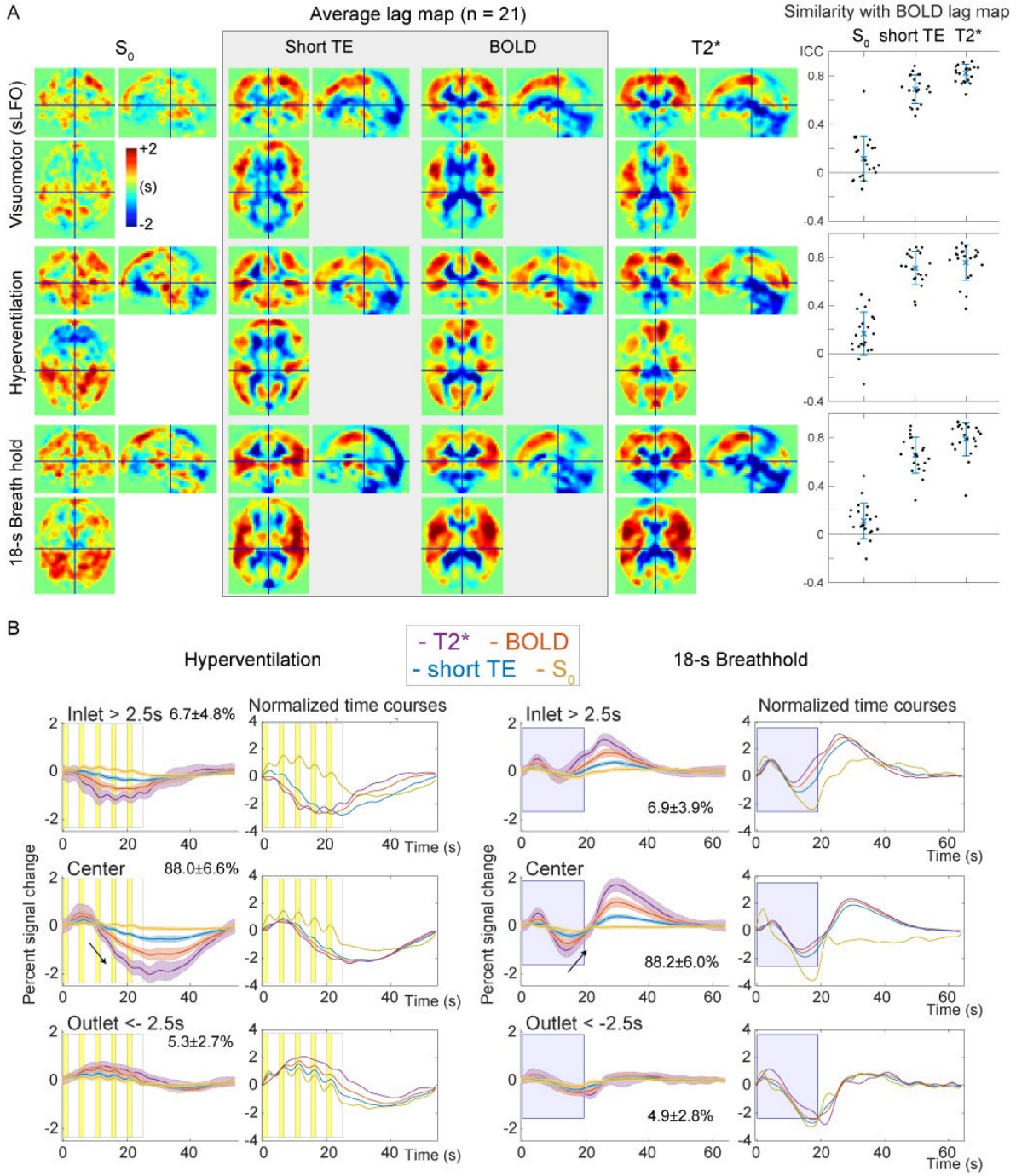

Fig. 9. Analysis of the signal components and the lag structure. (A) S_0 and T2* signals were interpolated based on multi-echo acquisitions at short and typical TEs for BOLD fMRI. The lag map created from the S_0 image shows a unique structure but fails to reflect the arterial and venous structures that are consistently found in the BOLD lag map. Using the T2*-weighted signals, the lag map changes upon respiratory

561 challenges, which should primarily reflect the modification of the perfusion pattern;
562 however, an interaction with the signal component is not excluded. The right panels
563 show intraclass correlation coefficients as a quantitative measure of within-participant
564 image similarity with the BOLD lag map, with error bars indicating 95% confidence
565 intervals. (B) Temporal profiles from the 3 vascular regions indicate an absence of
566 region effects in the S_0 signal, suggesting a globally uniform mechanism underlying
567 the S_0 response.

568 BOLD, blood oxygen level-dependent; ICC, interclass coefficient; TE, echo time;
569 fMRI, functional magnetic resonance imaging; sLFO, spontaneous low-frequency
570 oscillation

571

572 To further investigate the signal origin, we extracted the response in the
573 motor/premotor area activation peak, where NVC was expected to dominate (**Supp. Fig.**
574 **2A**). For this analysis, the group activation map from Experiment 1 was used to define the
575 regions-of-interest in order to avoid bias. We found high-frequency components
576 dominating the S_0 responses in comparison to the responses from larger regions shown in
577 **Figure 9B**. During hyperventilation, respiratory phase-related fluctuations were observed
578 with a signal decrease initiated by inhalation and followed by a positive deflection during
579 exhalation. The T2* signal also exhibited small fluctuations but with a different phase,
580 possibly dominated by the NVC component.

581 We conducted an additional analysis for the fast respiration-related non-BOLD
582 components. The spatial distribution of this response is shown in **Supp. Fig. 2B**.
583 Interestingly, there was a clear anterior-posterior segmentation of response polarity, with
584 the posterior regions presenting the opposite phase of the fast S_0 deflection by respiratory
585 maneuvers. Some additional symmetrical structures were found in deep-brain regions, near
586 the deep middle cerebral and inferior ventricular veins, implying a unique vascular
587 involvement. Importantly, this spatial pattern was not that of typical motion artifacts that
588 can accompany volitional respiration in spite of the careful instruction.

589 Finally, **Supp. Fig. 2C** shows the data from a subset of participants, obtained using a
590 different TR/flip-angle setting to manipulate the inflow effect. The T2* response was
591 smaller than that shown in **Fig. 2A**, presumably due to the short TR. The different TR also
592 contributed to the rich high-frequency components by the fast sampling rate. The slow S_0
593 change was also diminished, but the respiration-related fast component was relatively
594 preserved suggesting the absence of a strong inflow effect.

595 **4 Discussion**

596 The principal findings of this study are summarized as follows. First, based on the
597 instantaneous phase difference within the BOLD lag structure, we observed a small blood
598 flow velocity change selectively in the inlet region of the vasculature. Next, the complete
599 elimination of the lag structure reduced interindividual variance and spurious deactivation,
600 supporting our hypothesis that NVC could be observed more specifically by this
601 deperfusioning procedure. This finding is in agreement with the results of earlier work on
602 resting-state fMRI (Erdoğan *et al.*, 2016). Finally, the lag structures in the S_0 (or non-
603 BOLD) component did not correlate with that from T2*, either spatially or temporally. We
604 also found a vascular region-dependent change in the T2* sLFO, with a decreased
605 amplitude in the outlet part close to major veins, in contrast to the S_0 response that
606 remained constant; this finding replicates a previous observation in the raw BOLD signal
607 (Aso *et al.*, 2017*a*). The S_0 component exhibited a unique brain region-dependent response
608 to the respiratory phase, suggesting that certain perfusion parameters specifically contribute
609 to this component, but not the perfusion lag. Overall, the BOLD low-frequency phase
610 behaved as a deoxy-Hb-based virtual contrast agent in the present data, leaving a global
611 noise component for the fMRI analysis.

612 The observation that the velocity on the arterial side exhibits changes alongside
613 respiratory variations is consistent with the findings of previous reports using transcranial
614 Doppler ultrasonography (Malatino *et al.*, 1992; Poulin *et al.*, 1996). This information was
615 extracted from the BOLD lag structure, which itself presented autoregulatory response
616 consistent with earlier work (Murphy *et al.*, 2011). During the initial whole-brain CBV

increase in response to autoregulatory vasodilation, a sole increase in the inflow should first occur to meet the volume demand. It is therefore reasonable that this effect is absent in the outlet (i.e., the venous side of the gross vasculature). This observation seems to support the model in which the BOLD lag structure is derived from an axial non-uniformity in the vessels, already present in the inflow (Tong *et al.*, 2018). A distinct mechanism of the lag structure was also suggested by the diminished magnitude observed in the outlet side of the vasculature, since a CBF increase should evoke larger response in the downstream (Krings *et al.*, 1999).

It is unclear what proportion of this axial variation is systemic, i.e., originates from the autonomic loops, mediated by peripheral baro- or chemoreceptors. However, even when the neural activity is contributing to the sLFO time course as demonstrated previously (Aso *et al,* 2017), the resulting lag structure largely reflects the vasculature. In this work, we focused on non-neuronal mechanisms to account for the BOLD lag structure as much as possible, in the hope that it may ultimately help achieve a better understanding and provide improved modeling approaches of the fMRI signal.

4.1 Source of BOLD low-frequency oscillation signals

Previous studies on sLFOs have reported that both Hb species fluctuate, but with varying phase differences that are selectively found in the brain (Obrig *et al.*, 2000; Rayshubskiy *et al.*, 2014; Tgavalekos *et al.*, 2016). The observed fluctuations of total Hb density have been linked to CBV changes (Boas & Dale, 2005; Kennerley *et al.*, 2005; Kim & Ogawa, 2012), but interpretations for that of deoxy-Hb have rarely been provided. Only 1 series of studies by Fantini and colleagues directly addressed the possible axial variation of blood content such as oxygen saturation (Fantini, 2014). In support of the conventional theory, Rayshubskiy and colleagues reported, in their human intraoperative study, that slow Hb oscillations correlated with vasomotion in the superficial arteries (Rayshubskiy *et al.*, 2014). However, it remains unclear whether an equivalent vasomotion exists in the non-arterial vessels to fully account for the observed lag structure. Hence, it is worth considering other sources of deoxy-Hb variation.

645 The concept of vasomotion stems from an active diameter change in the precapillary
646 vessels, driving local velocity fluctuations, termed "flowmotion" (Intaglietta, 1990). This
647 flowmotion can reportedly accompany the fluctuation of local Hct that should affect deoxy-
648 Hb density (Fagrell *et al.*, 1980; Hudetz *et al.*, 1999). Another possible source for the
649 deoxy-Hb fluctuations is a change in SaO_2 that ranges from 94–98% in the artery
650 (Intaglietta *et al.*, 1996; Collins *et al.*, 2015). For example, the respiration-related BOLD
651 signal component is supposed to be mediated by the blood CO_2 level and pH, which can
652 shift the oxygen dissociation curve (Birn *et al.*, 2006; Chang & Glover, 2009*a*). These
653 parameters are considered to fluctuate in the blood as part of the autonomic loop, possibly
654 driving local vasomotion, which persists after denervation (Morita *et al.*, 1995). As
655 mentioned above, the phase difference between the 2 Hb species remains to be elucidated
656 (Sassaroli *et al.*, 2012), but those observations do substantiate an unstable deoxy-Hb supply
657 in brain tissues. Besides, such a signal component would have escaped detection in NVC
658 studies using trial averaging.

659 A signal origin intrinsic to the flowing blood may, as suggested by Tong and
660 colleagues, thus explain the constant phase difference among signals from different body
661 parts (Tong *et al.*, 2012, 2017). In the literature, an axial variation of the Hct in the brain
662 has indeed been suggested, in relation to both NVC (Kleinschmidt *et al.*, 1996; Siegel *et*
663 *al.*, 2003; Chen & Pike, 2009) and sLFOs (Fagrell *et al.*, 1980; Mayhew *et al.*, 1996).
664 Furthermore, the reduction in T2* LFO amplitude in the outlet side can be explained by the
665 high tissue deoxy-Hb density, which likely diminishes the proportional effect of intrinsic
666 deoxy-Hb fluctuations, unless the OEF is completely coupled to this variation. Importantly,
667 temporal dispersion alone would not fully account for the amplitude reduction, as it was
668 only found in the venous side, despite the fact that the lag structure was tracked both up-
669 and downstream from the global phase. These results provide good contrast with the stable
670 S_0 response, reflecting its insensitivity to oxygen saturation. Although it would be too
671 challenging to incorporate complex rheological parameters, a reconsideration of the
672 constant deoxy-Hb assumption may help improve BOLD signal modelling.

673 In the hyperventilation condition, we observed a fast response to each ventilation
674 cycle, accompanying blood pressure changes. This is consistent with reports using
675 optimized acquisition techniques (Dresel *et al.*, 2005; Pattinson *et al.*, 2009), supported by
676 anatomical (Simonyan & Jürgens, 2003), as well as electrophysiological (Radna &
677 MacLean, 1981) studies. The premotor peak at coordinates [+56, 0, 40] was also very close
678 to the reported activation site for volitional respiration (McKay *et al.*, 2008). Although the
679 effect of respiratory movement cannot be fully excluded, the spatial pattern in **Supp. Fig.**
680 **2B** is not that of a typical motion artifact centered on the brain surface (Krings *et al.*, 2001).
681 In healthy participants, inhalation increases systemic venous return through decreased
682 intrathoracic pressure, causing an elevation of cardiac output with some delay. In contrast,
683 exhalation is considered to cause CBV increases through elevated cerebral venous pressure.
684 To our knowledge, the timing order of these events has not been studied at the precision of
685 the current data; further studies are needed to determine the source of this S_0 fluctuation
686 (Yen *et al.*, 2017). The only available clue in our results is the spatial distribution, such as
687 the interesting anterior-posterior segmentation (resembling the unique "S_0 lag structure" in
688 **Fig. 9a**) or the symmetrical pattern in the deep brain structures. Nonetheless, some
689 mechanical effects of the respiratory act on the fluid dynamics likely exist, causing this
690 spatially heterogeneous S_0 deflection.

691 **4.2 Lag structure as noise**

692 Based on the assumption that the global signal fluctuation is the sum of all variations by
693 NVC, its elimination by GSR has been considered to negatively bias the results (Caballero-
694 Gaudes & Reynolds, 2017). However, as noted by Aguirre and others, there are cases
695 where GSR yields interpretable results even in the absence of global motion artifacts
696 (Aguirre *et al.*, 1998). The rise in popularity of rs-fMRI since 2005 has led to this issue
697 resurfacing in a different form. A variation in GSR, in which the time series extracted from
698 a set of regions-of-interest (whole brain, white matter, and cerebrospinal fluid) are
699 removed, has become a *de facto* standard. It is indeed computationally closer to our
700 deperfusioning in that the regional phase difference is somehow tolerated. However,
701 because this practice lacks a strong theoretical background (Chang *et al.*, 2009; Liu *et al.*,

2017), currently, the identification and elimination of bodily movements and physiological noise are more widely recommended. There are various approaches to this end, such as simultaneous physiological measurements (Chang & Glover, 2009*b*), as well as data-driven methods that only use fMRI data (Smith *et al.*, 2013). To date, however, objective criteria for distinguishing neural activity from noise components remains an issue (Salimi-Khorshidi *et al.*, 2014).

In the present study, the lag structure was treated as a broadly distributed, structured noise for fMRI. Indeed, it can be partly eliminated by sophisticated denoising techniques (Aso *et al.*, 2017*a*). However, the specificity of lag mapping in isolating information on a purely vascular origin remains unclear. For example, measurements of velocity changes critically depend on a recursive lag-tracking method that incorporates the gradual change in LFO over regions (Tong & Frederick, 2014). Adaptation for changes in the waveform that may arise from different paths of the blood was demonstrated to increase the reproducibility of the lag map (Aso *et al.*, 2017*a*). However, as the changes in waveform can also reflect NVC, removing the whole lag structure may lead to type II errors in the fMRI results. Hence, the favorable impacts of the deperfusioning procedure that we observed on the fMRI results are clearly insufficient to prove the advantage of this technique and require further confirmation.

Importantly, the detection of the lag structure itself largely depends on the data quality, especially in terms of head movement. When a head movement results in a synchronized deflection that exceeds the LFO amplitude, it would obscure the phase variation. However, it can be also questioned if the correlational structure of neural activity is reliably detected from such motion-contaminated data. In general, NVC should have a limited spatial extent and signal magnitude without time-locked averaging (Power *et al.*, 2012). In turn, successful tracking of a lag structure may even be considered as evidence of "clean" data. The elimination of this identified lag structure can be a relatively straightforward approach to reduce structured physiological noise (Caballero-Gaudes & Reynolds, 2017).

In conclusion, by investigating various aspects of the BOLD sLFO, we compiled supporting evidence for a component intrinsic to flowing blood that has been a focus of interest in earlier works (Tong *et al.*, 2017). To establish a framework by which the fMRI signal can be fully modeled, more detailed characterization of the lag structure as part of the "global noise" is needed (Glasser *et al.*, 2018).

5 Conflict of Interest

The authors declare that the research was conducted in the absence of any commercial or financial relationships that could be construed as a potential conflict of interest.

6 Author Contributions

All authors provided approval of the final version of the manuscript to be published. TA contributed to concept and design of this research, data analysis and interpretation, and drafting of the manuscript. SU contributed to data acquisition and drafting of the manuscript. SU, HF, and TM contributed to data interpretation and review of the final draft.

7 Funding

This study was supported by a Grant-in-Aid for Scientific Research on Innovative Areas (Non-linear Neuro-oscillology: Towards Integrative Understanding of Human Nature, JP15H05875) to TA and JP16H06395 and JP16H06397 to TM from the Japan Society for the Promotion of Science.

8 Acknowledgments

We would like to thank Editage (www.editage.jp) for English language editing.

9 Data Availability Statement

The datasets analyzed for this study can be provided upon request.

10 References

Aguirre GK, Zarahn E & D'Esposito M (1998). The inferential impact of global signal covariates in functional neuroimaging analyses. *NeuroImage* **8,** 302–306.

Amemiya S, Kunimatsu A, Saito N & Ohtomo K (2013). Cerebral Hemodynamic Impairment: Assessment with Resting-State Functional MR Imaging. *Radiology* **270,** 1–8.

Amemiya S, Takao H, Hanaoka S & Ohtomo K (2016). Global and structured waves of rs-fMRI signal identified as putative propagation of spontaneous neural activity. *NeuroImage* **133,** 331–340.

An H & Lin W (2002). Cerebral oxygen extraction fraction and cerebral venous blood volume measurements using MRI: Effects of magnetic field variation. *Magnetic Resonance in Medicine* **47,** 958–966.

Anderson JS, Druzgal TJ, Lopez-Larson M, Jeong E, Desai K & Yurgelun-Todd D (2011). Network anticorrelations, global regression, and phase-shifted soft tissue correction. *Human brain mapping* **32,** 919–934.

Aso T, Jiang G, Urayama S & Fukuyama H (2017*a*). A Resilient, Non-neuronal Source of the Spatiotemporal Lag Structure Detected by BOLD Signal-Based Blood Flow Tracking. *Frontiers in Neuroscience* **11,** 256.

Aso T, Urayama S & Fukuyama H (2017*b*). Temporal variation of cerebrovascular transit time measured by BOLD-based time lag mapping. In *Proceedings of the 25rd Annual Meeting of ISMRM*. Honolulu.

Birn RM, Diamond JB, Smith M a. & Bandettini P a. (2006). Separating respiratory-variation-related fluctuations from neuronal-activity-related fluctuations in fMRI. *NeuroImage* **31,** 1536–1548.

Birn RM, Murphy K & Bandettini PA (2008). The effect of respiration variations on independent component analysis results of resting state functional connectivity. *Human Brain Mapping* **29,** 740–750.

Blockley NP, Driver ID, Francis ST, Fisher JA & Gowland PA (2011). An improved method for acquiring cerebrovascular reactivity maps. *Magnetic Resonance in Medicine* **65,** 1278–1286.

Boas DA & Dale AM (2005). Simulation study of magnetic resonance imaging–guided cortically constrained diffuse optical tomography of human brain function. *Applied Optics* **44,** 1957.

Buxton RB (2013). The physics of functional magnetic resonance imaging (fMRI). *Reports on Progress in Physics* **76,** 096601.

Byrge L & Kennedy DP (2018). Identifying and characterizing systematic temporally-lagged BOLD artifacts. *NeuroImage* **171,** 376–392.

Caballero-Gaudes C & Reynolds RC (2017). Methods for cleaning the BOLD fMRI signal. *NeuroImage* **154,** 128–149.

Chang C, Cunningham JP & Glover GH (2009). Influence of heart rate on the BOLD signal: The cardiac response function. *NeuroImage* **44,** 857–869.

Chang C & Glover GH (2009*a*). Relationship between respiration, end-tidal CO2, and BOLD signals in resting-state fMRI. *NeuroImage* **47,** 1381–1393.

Chang C & Glover GH (2009*b*). Effects of model-based physiological noise correction on default mode network anti-correlations and correlations. *NeuroImage* **47,** 1448–1459.

Chen JJ & Pike GB (2009). BOLD-specific cerebral blood volume and blood flow changes during neuronal activation in humans. *NMR in biomedicine* **22,** 1054–1062.

Christen T, Jahanian H, Ni WW, Qiu D, Moseley ME & Zaharchuk G (2015). Noncontrast mapping of arterial delay and functional connectivity using resting-state functional MRI: A study in Moyamoya patients. *Journal of Magnetic Resonance Imaging* **41,** 424–430.

Cohen ER, Ugurbil K & Kim S-G (2002). Effect of basal conditions on the magnitude and dynamics of the blood oxygenation level-dependent fMRI response. *Journal of cerebral blood flow and metabolism : official journal of the International Society of Cerebral Blood Flow and Metabolism* **22,** 1042–1053.

Collins J-A, Rudenski A, Gibson J, Howard L & O'Driscoll R (2015). Relating oxygen partial pressure, saturation and content: the haemoglobin-oxygen dissociation curve. *Breathe (Sheffield, England)* **11,** 194–201.

Dresel C, Castrop F, Haslinger B, Wohlschlaeger AM, Hennenlotter A & Ceballos-Baumann AO (2005). The functional neuroanatomy of coordinated orofacial movements: Sparse sampling fMRI of whistling. *NeuroImage* **28,** 588–597.

Erdoğan SB, Tong Y, Hocke LM, Lindsey KP & Blaise deB Frederick (2016). Correcting for Blood Arrival Time in Global Mean Regression Enhances Functional Connectivity Analysis of Resting State fMRI-BOLD Signals. *Frontiers in human neuroscience* **10,** 311.

Fagrell B, Fronek A & Intaglietta M (1977). A microscope-television system for studying flow velocity in human skin capillaries. *The American journal of physiology* **233,** H318-21.

Fagrell B, Intaglietta M & Ostergren J (1980). Relative hematocrit in human skin capillaries and its relation to capillary blood flow velocity. *Microvascular research* **20,** 327–335.

Fantini S (2014). Dynamic model for the tissue concentration and oxygen saturation of hemoglobin in relation to blood volume, flow velocity, and oxygen consumption: Implications for functional neuroimaging and coherent hemodynamics spectroscopy (CHS). *NeuroImage* **85,** 202–221.

Feinberg D a, Moeller S, Smith SM, Auerbach E, Ramanna S, Gunther M, Glasser MF, Miller KL, Ugurbil K & Yacoub E (2010). Multiplexed echo planar imaging for

830 sub-second whole brain FMRI and fast diffusion imaging. *PloS one* **5,** e15710.

831 Freire L & Mangin JF (2001). Motion correction algorithms may create spurious brain
832 activations in the absence of subject motion. *NeuroImage* **14,** 709–722.

833 Friston KJ, Glaser DE, Henson RNA, Kiebel S, Phillips C & Ashburner J (2002). Classical
834 and Bayesian inference in neuroimaging: Applications. *NeuroImage* **16,** 484–512.

835 Giller CA, Hatab MR & Giller AM (1999). Oscillations in cerebral blood flow detected
836 with a transcranial Doppler index. *Journal of cerebral blood flow and metabolism :*
837 *official journal of the International Society of Cerebral Blood Flow and Metabolism*
838 **19,** 452–459.

839 Glasser MF, Coalson TS, Bijsterbosch JD, Harrison SJ, Harms MP, Anticevic A, Van
840 Essen DC & Smith SM (2018). Using temporal ICA to selectively remove global
841 noise while preserving global signal in functional MRI data. *NeuroImage* **181,** 692–
842 717.

843 Guyton AC & Harris JW (1951). Pressoreceptor-autonomic oscillation; a probable cause of
844 vasomotor waves. *The American journal of physiology* **165,** 158–166.

845 Herman P, Sanganahalli BG & Hyder F (2009). Multimodal Measurements of Blood
846 Plasma and Red Blood Cell Volumes during Functional Brain Activation. *Journal*
847 *of Cerebral Blood Flow & Metabolism* **29,** 19–24.

848 Hillman EMC (2014). Coupling Mechanism and Significance of the BOLD Signal: A
849 Status Report. *Annual Review of Neuroscience* **37,** 161–181.

850 Hoge R, Atkinson J, Gill B, Crelier G & Marrett S (1999). Investigation of BOLD signal
851 dependence on cerebral blood flow and oxygen consumption: The …. *Magnetic*
852 *Resonance in Medicine* **863,** 849–863.

853 Hoiland RL, Tymko MM, Bain AR, Wildfong KW, Monteleone B & Ainslie PN (2016).
854 Carbon dioxide-mediated vasomotion of extra-cranial cerebral arteries in humans: a
855 role for prostaglandins? *J Physiol* **594,** 3463–3481.

856 Hudetz a G, Wood JD, Biswal BB, Krolo I & Kampine JP (1999). Effect of hemodilution
857 on RBC velocity, supply rate, and hematocrit in the cerebral capillary network.
858 *Journal of applied physiology (Bethesda, Md : 1985)* **87,** 505–509.

859 Intaglietta M (1990). Vasomotion and flowmotion: physiological mechanisms and clinical
860 evidence. *Vascular Medicine Review* **1,** 101–112.

861 Intaglietta M, Johnson PC & Winslow RM (1996). Microvascular and tissue oxygen
862 distribution. *Cardiovascular research* **32,** 632–643.

863 Julien C (2006). The enigma of Mayer waves: Facts and models. *Cardiovascular research*
864 **70,** 12–21.

865 Katura T, Tanaka N, Obata A, Sato H & Maki A (2006). Quantitative evaluation of
866 interrelations between spontaneous low-frequency oscillations in cerebral
867 hemodynamics and systemic cardiovascular dynamics. *NeuroImage* **31,** 1592–1600.

Kennerley AJ, Berwick J, Martindale J, Johnston D, Papadakis N & Mayhew JE (2005). Concurrent fMRI and Optical Measures for the Investigation of the Hemodynamic Response Function. **365,** 354–365.

Khalil AA, Villringer K, Filleböck V, Hu J-Y, Rocco A, Fiebach JB & Villringer A (2018). Non-invasive monitoring of longitudinal changes in cerebral hemodynamics in acute ischemic stroke using BOLD signal delay. *Journal of Cerebral Blood Flow & Metabolism*0271678X1880395.

Killip T (1962). Oscillation of blood flow and vascular resistance during Mayer waves. *Circulation research* **11,** 987–993.

Kim JH & Ress D (2016). Arterial impulse model for the BOLD response to brief neural activation. *NeuroImage* **124,** 394–408.

Kim S-G & Ogawa S (2012). Biophysical and physiological origins of blood oxygenation level-dependent fMRI signals. *Journal of Cerebral Blood Flow & Metabolism* **32,** 1188–1206.

Kleinschmidt A, Obrig H, Requardt M, Merboldt K-D, Dirnagl U, Villringer A & Frahm J (1996). Simultaneous Recording of Cerebral Blood Oxygenation Changes during Human Brain Activation by Magnetic Resonance Imaging and Near-Infrared Spectroscopy. *Journal of Cerebral Blood Flow & Metabolism* **16,** 817–826.

Krings T, Erberich SG, Roessler F, Reul J & Thron A (1999). MR blood oxygenation level-dependent signal differences in parenchymal and large draining vessels: implications for functional MR imaging. *AJNR American journal of neuroradiology* **20,** 1907–1914.

Krings T, Reinges MHT, Erberich S, Kemeny S, Rohde V, Spetzger U, Korinth M, Willmes K, Gilsbach JM & Thron A (2001). Functional MRI for presurgical planning: problems, artefacts, and solution strategies. *J Neurol Neurosurg Psychiatry* **70,** 749.

Kumar V, Croxson PL & Simonyan K (2016). Structural Organization of the Laryngeal Motor Cortical Network and Its Implication for Evolution of Speech Production. *Journal of Neuroscience* **36,** 4170–4181.

Kundu P, Inati SJ, Evans JW, Luh W-M & Bandettini PA (2012). Differentiating BOLD and non-BOLD signals in fMRI time series using multi-echo EPI. *NeuroImage* **60,** 1759–1770.

Liu TT, Nalci A & Falahpour M (2017). The global signal in fMRI: Nuisance or Information? *NeuroImage* **150,** 213–229.

Lv Y, Margulies DS, Cameron Craddock R, Long X, Winter B, Gierhake D, Endres M, Villringer K, Fiebach J & Villringer A (2013). Identifying the perfusion deficit in acute stroke with resting-state functional magnetic resonance imaging. *Annals of Neurology* **73,** 136–140.

Malatino LS, Bellofiore S, Costa MP, Lo Manto G, Finocchiaro F & Di Maria GU (1992).

907 Cerebral blood flow velocity after hyperventilation-induced vasoconstriction in
908 hypertensive patients. *Stroke* **23,** 1728–1732.

909 Mayhew JEW, Askew S, Zheng Y, Porrill J, Westby GWMW, Redgrave P, Rector DM &
910 Harper RM (1996). Cerebral Vasomotion: A 0.1-Hz Oscillation in Reflected Light
911 Imaging of Neural Activity. *NeuroImage* **4,** 183–193.

912 Mazaika PK, Hoeft F, Glover GH & Reiss AL (2009). Methods and Software for fMRI
913 Analysis of Clinical Subjects. *NeuroImage* **47,** S58.

914 McKay LC, Adams L, Frackowiak RSJ & Corfield DR (2008). A bilateral cortico-bulbar
915 network associated with breath holding in humans, determined by functional
916 magnetic resonance imaging. *NeuroImage* **40,** 1824–1832.

917 Morita Y, Hardebo JE & Bouskela E (1995). Influence of cerebrovascular sympathetic,
918 parasympathetic, and sensory nerves on autoregulation and spontaneous
919 vasomotion. *Acta Physiol Scand* **154,** 121–130.

920 Murphy K, Birn RM & Bandettini PA (2013). Resting-state fMRI confounds and cleanup.
921 *NeuroImage* **80,** 349–359.

922 Murphy K, Harris AD & Wise RG (2011). Robustly measuring vascular reactivity
923 differences with breath-hold: Normalising stimulus-evoked and resting state BOLD
924 fMRI data. *NeuroImage* **54,** 369–379.

925 Ni L, Li J, Li W, Zhou F, Wang F, Schwarz CG, Liu R, Zhao H, Wu W, Zhang X, Li M,
926 Yu H, Zhu B, Villringer A, Zang Y, Zhang B, Lv Y & Xu Y (2017). The value of
927 resting-state functional MRI in subacute ischemic stroke: comparison with dynamic
928 susceptibility contrast-enhanced perfusion MRI. *Scientific Reports* **7,** 41586.

929 Nikulin V V, Fedele T, Mehnert J, Lipp A, Noack C, Steinbrink J & Curio G (2014).
930 Monochromatic Ultra-Slow (~0.1Hz) Oscillations in the human
931 electroencephalogram and their relation to hemodynamics. *NeuroImage* **97,** 71–80.

932 Nishida S, Aso T, Takaya S, Takahashi Y, Kikuchi T, Funaki T, Yoshida K, Okada T,
933 Kunieda T, Togashi K, Fukuyama H & Miyamoto S (2018). Resting-state
934 Functional Magnetic Resonance Imaging Identifies Cerebrovascular Reactivity
935 Impairment in Patients With Arterial Occlusive Diseases: A Pilot Study.
936 *Neurosurgery*; DOI: 10.1093/neuros/nyy434.

937 Obrig H, Neufang M, Wenzel R, Kohl M, Steinbrink J, Einhäupl K & Villringer A (2000).
938 Spontaneous Low Frequency Oscillations of Cerebral Hemodynamics and
939 Metabolism in Human Adults. *NeuroImage* **12,** 623–639.

940 Ogawa S, Menon RS, Kim SG & Ugurbil K (1998). On the characteristics of functional
941 magnetic resonance imaging of the brain. *AnnuRevBiophysBiomolStruct* **27,** 447–
942 474.

943 Pattinson KTS, Governo RJ, MacIntosh BJ, Russell EC, Corfield DR, Tracey I & Wise RG
944 (2009). Opioids Depress Cortical Centers Responsible for the Volitional Control of
945 Respiration. *Journal of Neuroscience* **29,** 8177–8186.

Poline JB, Worsley KJ, Evans AC & Friston KJ (1997). Combining spatial extent and peak intensity to test for activations in functional imaging. *NeuroImage* **5,** 83–96.

Posse S, Wiese S, Gembris D, Mathiak K, Kessler C, Grosse-Ruyken ML, Elghahwagi B, Richards T, Dager SR & Kiselev VG (1999). Enhancement of BOLD-contrast sensitivity by single-shot multi-echo functional MR imaging. *Magnetic resonance in medicine* **42,** 87–97.

Poulin MJ, Liang PJ & Robbins PA (1996). Dynamics of the cerebral blood flow response to step changes in end-tidal PCO2 and PO2 in humans. *Journal of Applied Physiology* **81,** 1084–1095.

Power JD, Barnes K a., Snyder AZ, Schlaggar BL & Petersen SE (2012). Spurious but systematic correlations in functional connectivity MRI networks arise from subject motion. *NeuroImage* **59,** 2142–2154.

Power JD, Plitt M, Laumann TO & Martin A (2017). Sources and implications of whole-brain fMRI signals in humans. *NeuroImage* **146,** 609–625.

Radna RJ & MacLean PD (1981). Vagal elicitation of respiratory-type and other unit responses in striopallidum of squirrel monkeys. *Brain Research* **213,** 29–44.

Rayshubskiy A, Wojtasiewicz TJ, Mikell CB, Bouchard MB, Timerman D, Youngerman BE, McGovern RA, Otten ML, Canoll P, McKhann GM & Hillman EMC (2014). Direct, intraoperative observation of ~0.1Hz hemodynamic oscillations in awake human cortex: Implications for fMRI. *NeuroImage* **87,** 323–331.

Rostrup E, Knudsen GM, Law I, Holm S, Larsson HBW & Paulson OB (2005). The relationship between cerebral blood flow and volume in humans. *NeuroImage* **24,** 1–11.

Salimi-Khorshidi G, Douaud G, Beckmann CF, Glasser MF, Griffanti L & Smith SM (2014). Automatic denoising of functional MRI data: Combining independent component analysis and hierarchical fusion of classifiers. *NeuroImage* **90,** 449–468.

Sassaroli A, Pierro M, Bergethon PR & Fantini S (2012). Low-frequency spontaneous oscillations of cerebral hemodynamics investigated with near-infrared spectroscopy: A review. *IEEE Journal on Selected Topics in Quantum Electronics* **18,** 1478–1492.

Satow T, Aso T, Nishida S, Komuro T, Ueno T, Oishi N, Nakagami Y, Odagiri M, Kikuchi T, Yoshida K, Ueda K, Kunieda T, Murai T, Miyamoto S & Fukuyama H (2017). Alteration of Venous Drainage Route in Idiopathic Normal Pressure Hydrocephalus and Normal Aging. *Frontiers in Aging Neuroscience*; DOI: 10.3389/fnagi.2017.00387.

Satterthwaite TD, Elliott MA, Gerraty RT, Ruparel K, Loughead J, Calkins ME, Eickhoff SB, Hakonarson H, Gur RC, Gur RE & Wolf DH (2013). An improved framework for confound regression and filtering for control of motion artifact in the preprocessing of resting-state functional connectivity data. *NeuroImage* **64,** 240–256.

985 Siegel AM, Culver JP, Mandeville JB & Boas DA (2003). Temporal comparison of
986 functional brain imaging with diffuse optical tomography and fMRI during rat
987 forepaw stimulation. *Physics in medicine and biology* **48,** 1391–1403.

988 Simonyan K & Jürgens U (2003). Efferent subcortical projections of the laryngeal
989 motorcortex in the rhesus monkey. *Brain Research* **974,** 43–59.

990 Smith SM et al. (2013). Resting-state fMRI in the Human Connectome Project.
991 *NeuroImage* **80,** 144–168.

992 Smith SM, Jenkinson M, Woolrich MW, Beckmann CF, Behrens TEJ, Johansen-Berg H,
993 Bannister PR, De Luca M, Drobnjak I, Flitney DE, Niazy RK, Saunders J, Vickers
994 J, Zhang Y, De Stefano N, Brady JM & Matthews PM (2004). Advances in
995 functional and structural MR image analysis and implementation as FSL.
996 *NeuroImage* **23 Suppl 1,** S208-19.

997 Taylor Webb J, Ferguson M a., Nielsen J a. & Anderson JS (2013). BOLD granger
998 causality reflects vascular anatomy. *PLoS ONE* **8,** 1–19.

999 Tgavalekos KT, Kainerstorfer JM, Sassaroli A & Fantini S (2016). Blood-pressure-induced
1000 oscillations of deoxy- and oxyhemoglobin concentrations are in-phase in the healthy
1001 breast and out-of-phase in the healthy brain. *Journal of Biomedical Optics* **21,**
1002 101410.

1003 Thomas DL, Lythgoe MF, Pell GS, Calamante F & Ordidge RJ (2000). The measurement
1004 of diffusion and perfusion in biological systems using magnetic resonance imaging.
1005 *Physics in medicine and biology* **45,** R97-138.

1006 Tian F, Niu H, Khan B, Alexandrakis G, Behbehani K & Liu H (2011). Enhanced
1007 Functional Brain Imaging by Using Adaptive Filtering and a Depth Compensation
1008 Algorithm in Diffuse Optical Tomography. *IEEE Transactions on Medical Imaging*
1009 **30,** 1239–1251.

1010 Tong Y & Frederick B deB (2014). Tracking cerebral blood flow in BOLD fMRI using
1011 recursively generated regressors. *Human brain mapping* **35,** 5471–5485.

1012 Tong Y, Hocke LM, Licata SC & Frederick B deB (2012). Low-frequency oscillations
1013 measured in the periphery with near-infrared spectroscopy are strongly correlated
1014 with blood oxygen level-dependent functional magnetic resonance imaging signals.
1015 *Journal of biomedical optics* **17,** 106004.

1016 Tong Y, Lindsey KP, Hocke LM, Vitaliano G, Mintzopoulos D & Frederick B deB (2017).
1017 Perfusion information extracted from resting state functional magnetic resonance
1018 imaging. *Journal of cerebral blood flow and metabolism : official journal of the*
1019 *International Society of Cerebral Blood Flow and Metabolism* **37,** 564–576.

1020 Tong Y, Yao JF, Chen JJ & Frederick B deB (2018). The resting-state fMRI arterial signal
1021 predicts differential blood transit time through the brain. *Journal of cerebral blood*
1022 *flow and metabolism : official journal of the International Society of Cerebral*
1023 *Blood Flow and Metabolism*271678X17753329.

Tuunanen PI & Kauppinen RA (2006). Effects of oxygen saturation on BOLD and arterial spin labelling perfusion fMRI signals studied in a motor activation task. *NeuroImage* **30,** 102–109.

Willie CK, Tzeng Y-C, Fisher JA & Ainslie PN (2014). Integrative regulation of human brain blood flow: Integrative regulation of human brain blood flow. *The Journal of Physiology* **592,** 841–859.

Winder AT, Echagarruga C, Zhang Q & Drew PJ (2017). Weak correlations between hemodynamic signals and ongoing neural activity during the resting state. *Nature neuroscience* **20,** 1761–1769.

Wise RG, Ide K, Poulin MJ & Tracey I (2004). Resting fluctuations in arterial carbon dioxide induce significant low frequency variations in BOLD signal. *NeuroImage* **21,** 1652–1664.

Wu CW, Gu H, Zou Q, Lu H, Stein EA & Yang Y (2012). TE-dependent spatial and spectral specificity of functional connectivity. *NeuroImage* **59,** 3075–3084.

Yablonskiy DA & Haacke EM (1994). Theory of NMR signal behavior in magnetically inhomogeneous tissues: the static dephasing regime. *Magnetic resonance in medicine* **32,** 749–763.

Yen CC-C, Papoti D & Silva AC (2017). Investigating the spatiotemporal characteristics of the deoxyhemoglobin-related and deoxyhemoglobin-unrelated functional hemodynamic response across cortical layers in awake marmosets. *NeuroImage* **7,** 83–88.

Zhu DC, Tarumi T, Khan MA & Zhang R (2015). Vascular coupling in resting-state fMRI: evidence from multiple modalities. *Journal of cerebral blood flow and metabolism : official journal of the International Society of Cerebral Blood Flow and Metabolism* **35,** 1910–1920.

11 Additional Information

11.1 Competing Interests

None of the authors has any conflicts of interests.

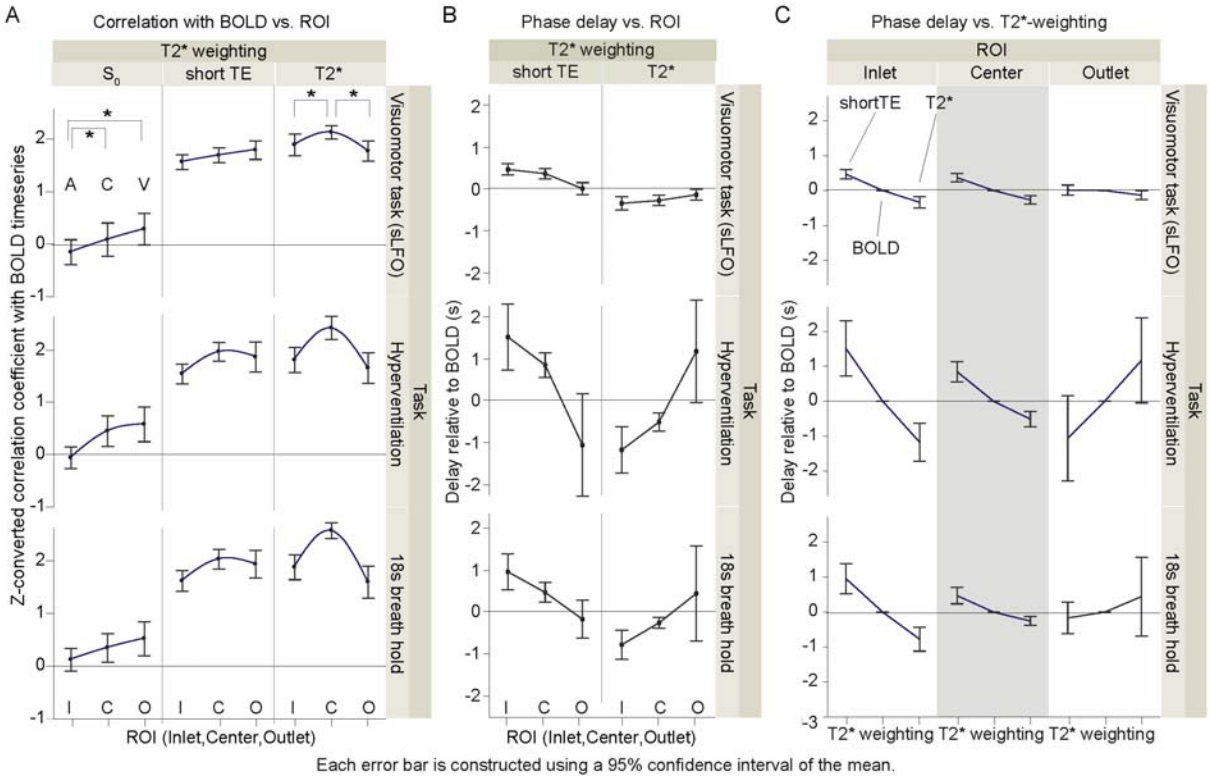

Supplementary Figure 1. A, Correlation analysis of the multi echo-derived signals extracted from the three vascular regions. Effects of vascular region was observed on both S_0 and T2* components, but in a different manner. **B,** Phase analysis of the low-frequency component below 0.1 Hz. Phase delay relative to BOLD time course was calculated for the two T2* weighted signals. Respiratory challenges enhanced the phase difference between S_0 and T2*. **C.** The same data as in B, but separately plotted for each region. Dissociation of the T2* and S_0 phase, as well as its interaction with the vascular region is evident. All these effects were small with spontaneous low-frequency fluctuation but enhanced in artificial oscillation by respiratory challenges.

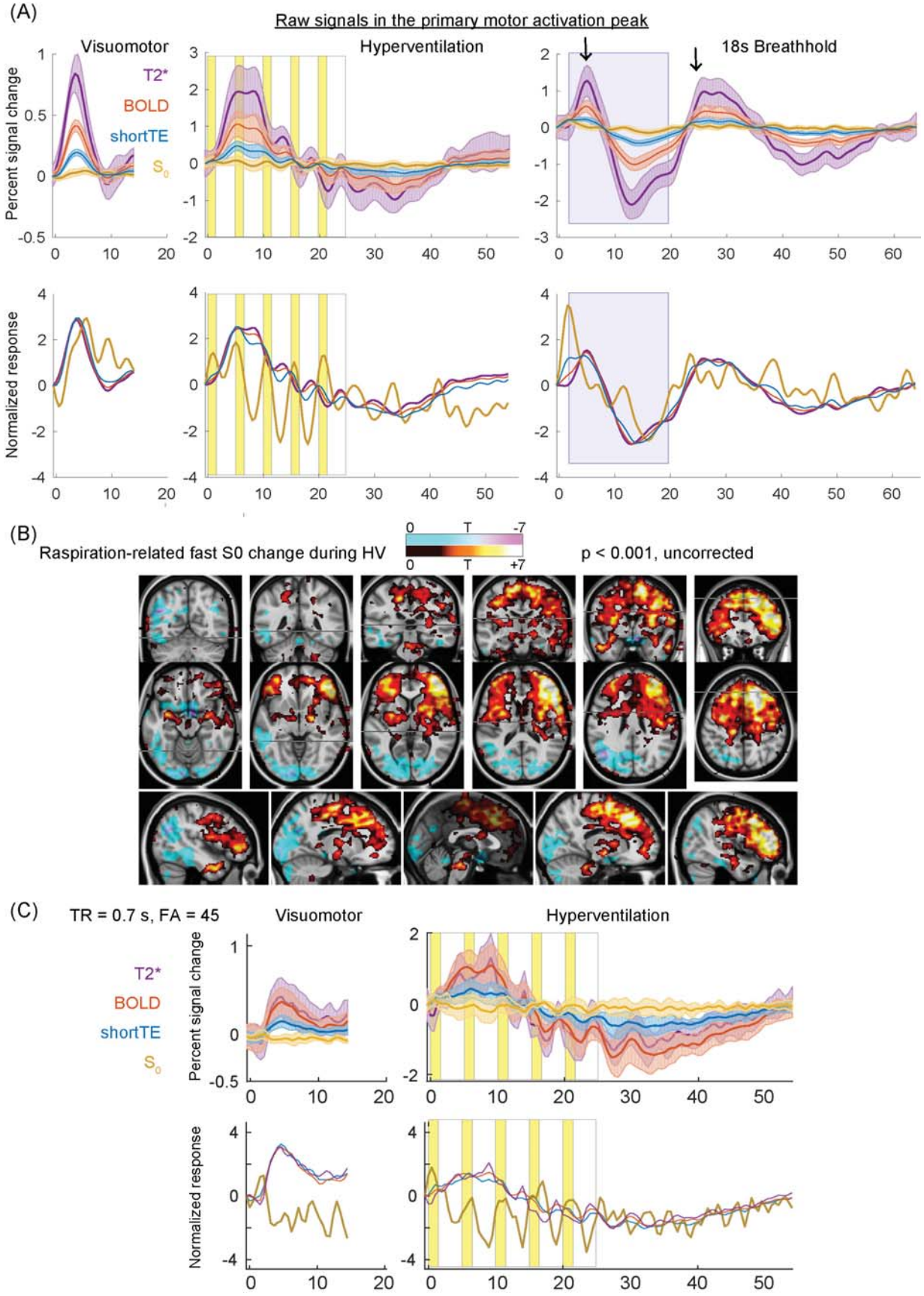
(A)
Raw signals in the primary motor activation peak
Visuomotor
Hyperventilation
18s Breathhold
T2*
BOLD
shortTE
S0
Percent signal change
Normalized response
(B)
Raspiration-related fast S0 change during HV
p < 0.001, uncorrected
(C)
TR = 0.7 s, FA = 45
Visuomotor
Hyperventilation
T2*
BOLD
shortTE
S0
Percent signal change
Normalized response

Supplementary Figure 2. A, Raw signal responses in the motor/premotor activation cluster for each task from Experiment 2. Time courses were resampled to a sampling interval of 0.5 s. Small but distinct responses were found in the non-BOLD or S_0 component but with a dominating fast component compared to the regional response, apparently independent of both the neurovascular coupling and hemoglobin fluctuations that accompany T2* changes. This response was roughly out of phase with the beat-to-beat mean arterial blood pressure shown in Fig. 3, although the blood pressure response was absent during the first two cycles. Arrows indicate the fluctuation corresponding to the neurovascular coupling modelled in the SPM analysis. **B.** Group SPM to assess the distribution of the respiratory phase-related fast fluctuation of S_0 during hyperventilation. A separate SPM analysis was performed by modeling the fast S_0 fluctuation only. An anterior-posterior segmentation is evident. In addition, there are small symmetrical structures along the major veins. **C.** Additional experiment from a subset of participants (N = 7) using a different set of repetition time/flip angle to manipulate the T1-inflow effect on the S_0 component. The overall S_0 response is lower than those shown in panel **A**, but the fast response to hyperventilation is preserved.